nature materials

SUPPLEMENTARY INFORMATION

https://doi.org/10.1038/s41563-019-0571-5

In the format provided by the authors and unedited.

Atomic-level tuning of Co–N–C catalyst for high-performance electrochemical H_2O_2 production

Euiyeon Jung[1,2,6], Heejong Shin[1,2,6], Byoung-Hoon Lee[1,2,6], Vladimir Efremov[3], Suhyeong Lee[3], Hyeon Seok Lee[1,2], Jiheon Kim[1,2], Wytse Hooch Antink[1,2], Subin Park[1,2], Kug-Seung Lee[4], Sung-Pyo Cho[5], Jong Suk Yoo[3]*, Yung-Eun Sung[1,2]* and Taeghwan Hyeon[1,2]*

[1]Center for Nanoparticle Research, Institute for Basic Science (IBS), Seoul, Republic of Korea. [2]School of Chemical and Biological Engineering, and Institute of Chemical Processes, Seoul National University, Seoul, Republic of Korea. [3]Department of Chemical Engineering, University of Seoul, Seoul, Republic of Korea. [4]Pohang Accelerator Laboratory (PAL), Pohang University of Science and Technology (POSTECH), Pohang, Republic of Korea. [5]National Center for Inter-University Research Facilities, Seoul National University, Seoul, Republic of Korea. [6]These authors contributed equally: Euiyeon Jung, Heejong Shin, Byoung-Hoon Lee. *e-mail: jsyoo84@uos.ac.kr; ysung@snu.ac.kr; thyeon@snu.ac.kr

[Supplementary Information]

Atomic-level tuning of Co-N-C catalyst for high-performance electrochemical H_2O_2 production

Euiyeon Jung[1,2,6], Heejong Shin[1,2,6], Byoung-Hoon Lee[1,2,6], Vladimir Efremov[3], Suhyeong Lee[3], Hyeon Seok Lee[1,2], Jiheon Kim[1,2], Wytse Hooch Antink[1,2], Subin Park[1,2], Kug-Seung Lee[4], Sung-Pyo Cho[5], Jong Suk Yoo[3]*, Yung-Eun Sung[1,2]* and Taeghwan Hyeon[1,2]*

[6]These authors contributed equally: Euiyeon Jung, Heejong Shin, Byoung-Hoon Lee

*Corresponding authors. Email: jsyoo84@uos.ac.kr (J.S.Y.); ysung@snu.ac.kr (Y.-E.S.); thyeon@snu.ac.kr (T.H.);

This file includes:

Supplementary Notes

Supplementary Figures 1 to 41

Table S1 to S4

References

The equilibrium potential for 2e- pathway ORR in alkaline media

The electrochemical H_2O_2 production is indicated by the ring current that gives an onset potential of ~ 0.8 V vs. RHE for the Co_1-NG(O) catalyst. It is a slightly higher onset potential than the thermodynamic limit of 0.76 V vs. RHE (in acidic media, given the pK_a values for the first and second ionization of H_2O_2 at 298 K, pK_{a1} = 11.69 and pK_{a2} = ~20, the predominant hydrogen peroxide species for pH < 12 is H_2O_2 whereas at pH > 12 it is HO_2^-)[1].

$$O_2 + 2H_2O + 4e^- \rightarrow 4OH^- \qquad E^o = 1.23 \text{ V vs. RHE} \qquad (1)$$

$$O_2 + H_2O + 2e^- \rightarrow HO_2^- + OH^- \qquad E^o = 0.76 \text{ V vs. RHE} \qquad (2)$$

Generally, the electrochemical H_2O_2 production can proceed through the $2e^-$ ORR process to convert O_2 to HO_2^- in alkaline electrolyte, in which E^o is the standard equilibrium potential calculated from the free energy of each reaction (H_2O_2 is in acidic electrolyte, but HO_2^- is its deprotonated anion in alkaline conditions). These could be attributed to a Nernst related potential shift due to the relatively low concentration of H_2O_2 in the electrolyte, which was also previously observed for the 2e- pathway ORR[2]. Recently, the McCloskey group showed that E = 0.825 V vs. RHE can be calculated assuming an HO_2^- concentration of 1 mM and O_2 pressure of 800 torr[2].

$$E = E^o - 0.059/2 \times \log([HO_2^-][OH^-]/p(O_2)) \qquad (3)$$

ORR mechanisms of carbonaceous catalysts in acidic and alkaline media

The bottleneck of the sluggish ORR mechanism is the transfer of electrons from the electrocatalyst surface to O_2 molecules. There are mainly two ORR mechanisms. One is the inner-sphere electron transfer mechanism that is facilitated through direct adsorption of O_2 molecules on the catalyst surface. The other one is known as the outer-sphere mechanism in which an electron is transferred to the solvated molecular O_2, $O_2 \cdot (H_2O)_n$, via hydroxyl species adsorbed on the catalyst surface[1].

In acidic electrolyte, outer-sphere mechanism is absent while both inner- and outer-sphere electron transfer mechanisms coexist in alkaline media[1]. Thus, without providing adsorption sites for O_2 molecules on inner sphere layer, catalysts cannot promote the ORR process in

acidic media. This is the reason why non-metal carbonaceous catalysts (NG(O), in our study) display little or no catalytic activity in acidic media, which has been reported in recent studies on the oxidized carbon nanotubes[3]. Therefore, it is necessary to promote the inner-sphere mechanism via molecular O_2 adsorption by introducing transition metal-based SACs in acidic media.

Likewise, in alkaline electrolyte, the presence of single atom metal centre on the carbon substrate can also promote additional massive ORR activities through inner-sphere mechanism. Thus, our Co_1-NG(O) catalyst can have significantly enhanced H_2O_2 production rate than any other non-metal carbon catalysts in alkaline media (Fig. 4c).

Feasibility of cobalt SACs for H_2O_2 production in wide pH range media

H. J. H. Fenton discovered that several metals have a strong catalytic power to generate highly reactive and disruptive hydroxyl radical (·OH) when they react with peroxide molecules. Iron has been the most used catalyst in the application for Fenton's reagent, since its catalytic reactivity is much higher than other transition metals in aqueous solution (pH = 3 ~ 8).

$$Fe^{2+} + H_2O_2 \rightarrow Fe^{3+} + \cdot OH + OH^- \quad (4)$$

$$Fe^{3+} + H_2O_2 \rightarrow Fe^{2+} + \cdot OOH + H^+ \quad (5)$$

Recently, the Wu group discussed that Fe-based catalysts suffered from poor stability due to the Fenton reaction, causing serious degradation of the catalysts, organic ionomers and the polymer membrane[4]. Alternatively, cobalt is less active to initiate Fenton reaction, but it also shows good catalytic performance for oxygen reduction. They suggested the atomically dispersed cobalt catalysts can mitigate Fenton reactions and replace the iron materials in fuel cell application. Thus, we have tried to design our catalysts for H_2O_2 production with cobalt atoms. Then, we compared the stability of our Co_1-NG(O) with that of Fe-based catalysts in 0.1 M $HClO_4$ electrolyte (Supplementary Fig. 36). It reveals that our electron-poor Co single atom site is more stable than common Fe-N_4 structure, and this Co atom is hardly leached out during the H_2O_2 production process. Likewise, the Wu group suggested another catalyst comprising Mn-N_4 structure which is highly stable and active for $4e^-$ ORR process[5]. However, cobalt SACs are more suitable for H_2O_2 production, as our theoretical calculation results

showed. Our Co_1-NG(O) catalyst reveals comparable mass activity for H_2O_2 production with other platinum SACs[6-8] in acidic media (Supplementary Fig. 39).

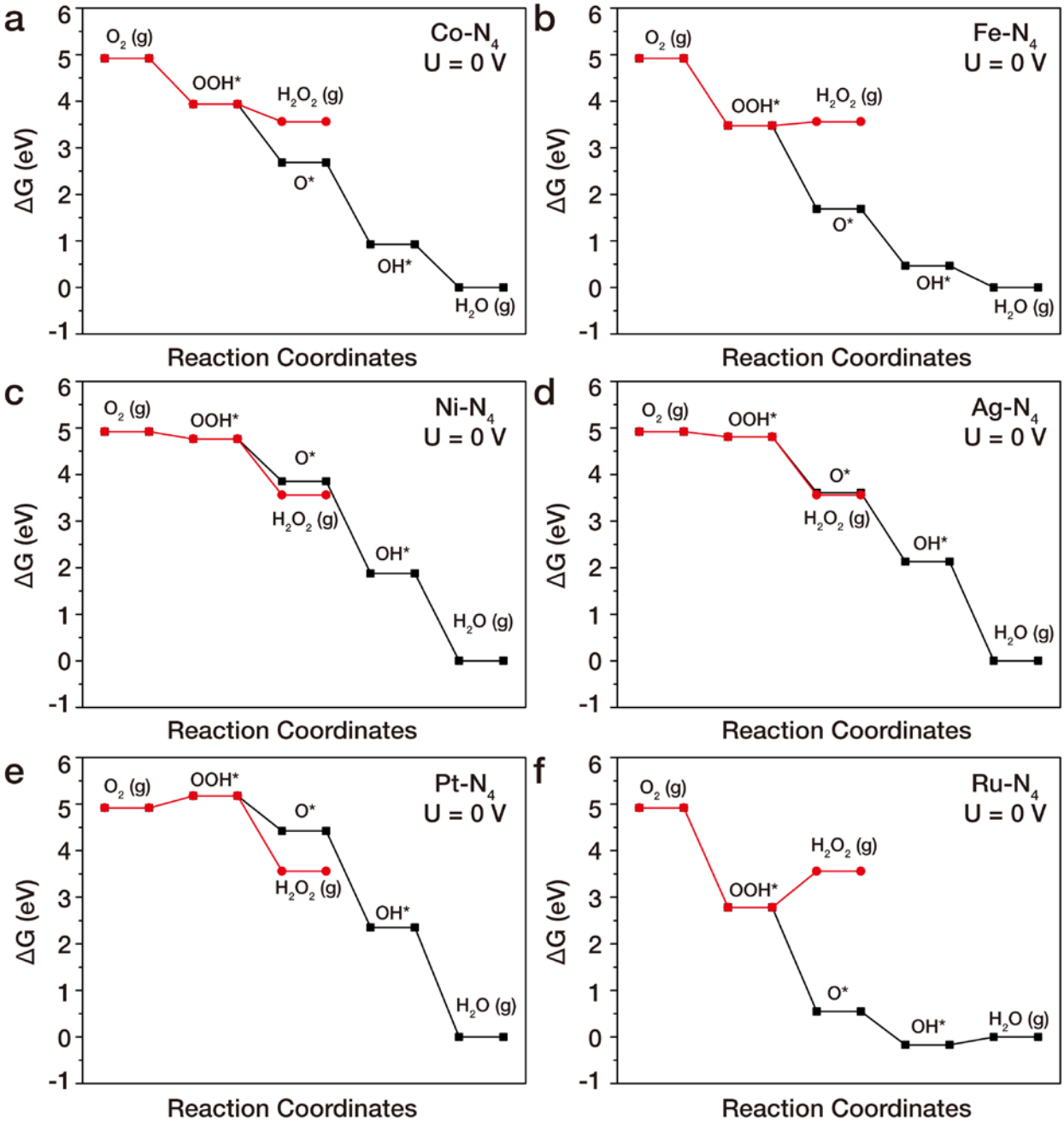

Supplementary Figure 1. Calculated reaction energetics of the oxygen reduction reaction to hydrogen peroxide (red) and water (black) on M-N_4/graphene (M = Co, Ni, Fe, Ag, Pt, Ru) at U = 0 V vs RHE.

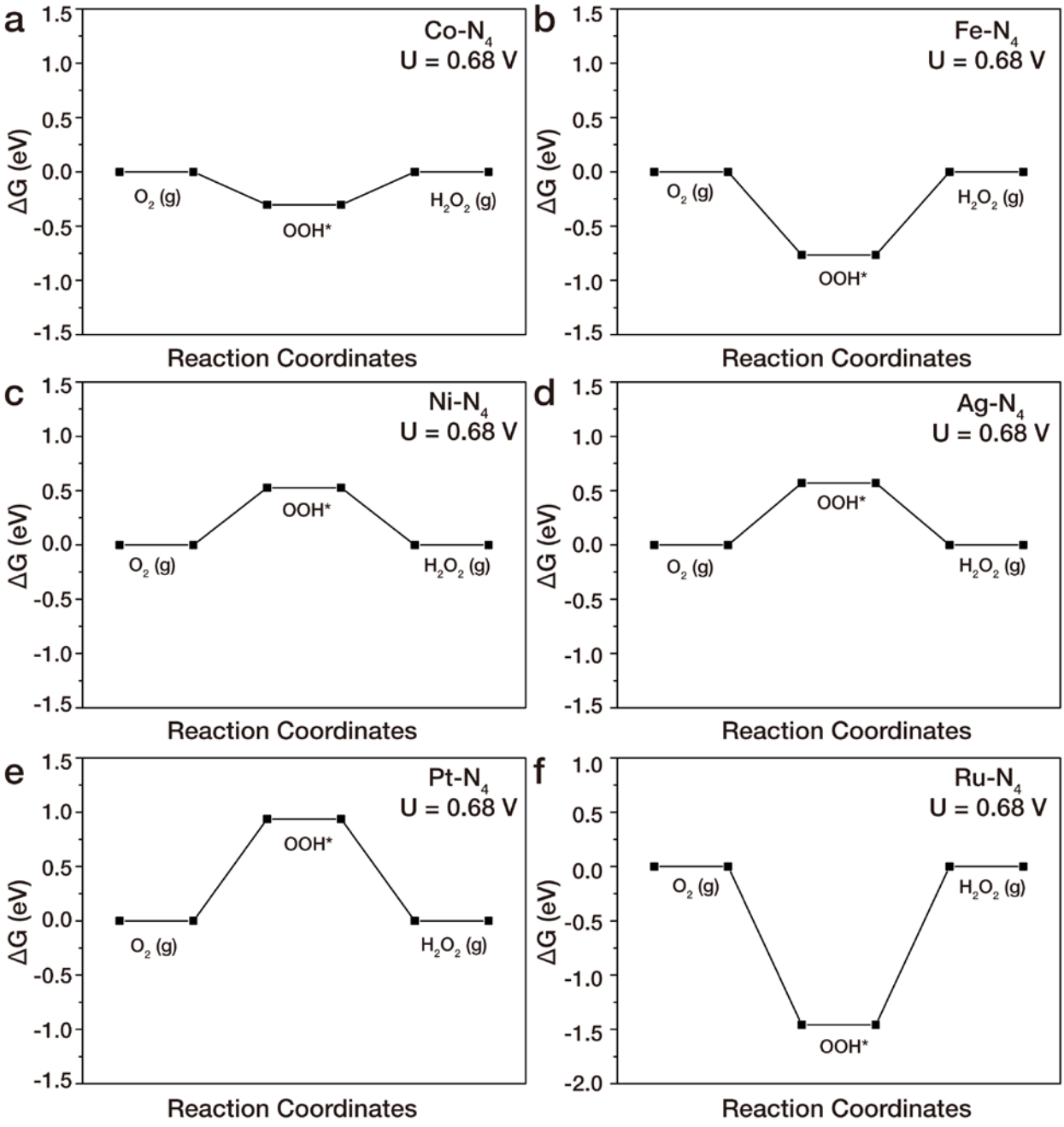

Supplementary Figure 2. Calculated reaction energetics of the oxygen reduction reaction to hydrogen peroxide on M-N_4/graphene (M = Co, Ni, Fe, Ag, Pt, Ru) at the equilibrium potential for H_2O_2 production (U = 0.68 V vs RHE).

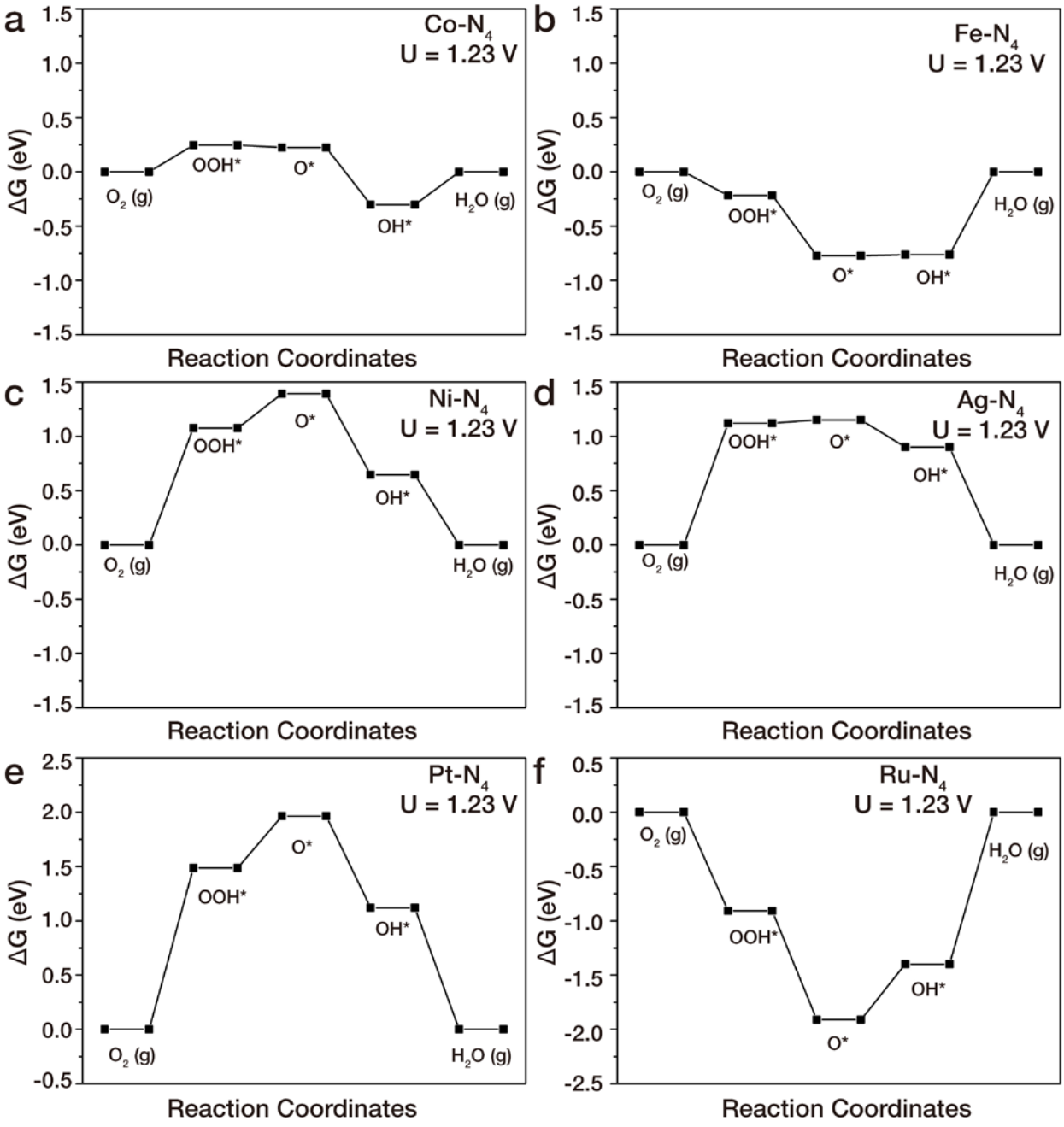

Supplementary Figure 3. Calculated reaction energetics of the oxygen reduction reaction to water on M-N_4/graphene (M = Co, Ni, Fe, Ag, Pt, Ru) at the equilibrium potential for H_2O production (U = 1.23 V vs RHE).

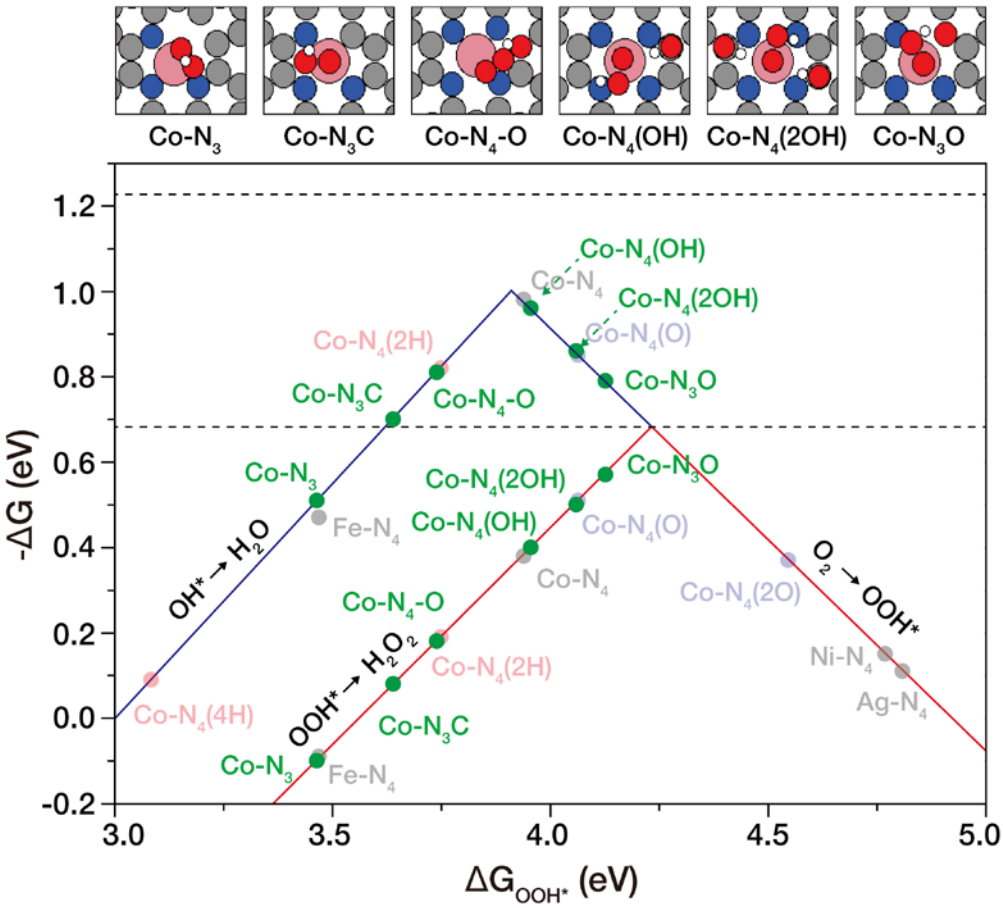

Supplementary Figure 4. Calculated catalytic activity volcano plots for the production of H_2O (black line) and H_2O_2 (red line) via the oxygen reduction reaction. Shaded data points are those shown in Fig. 1a. Green data points represent Co-N_4/graphene with different atomic structures as shown in the top schematic diagrams.

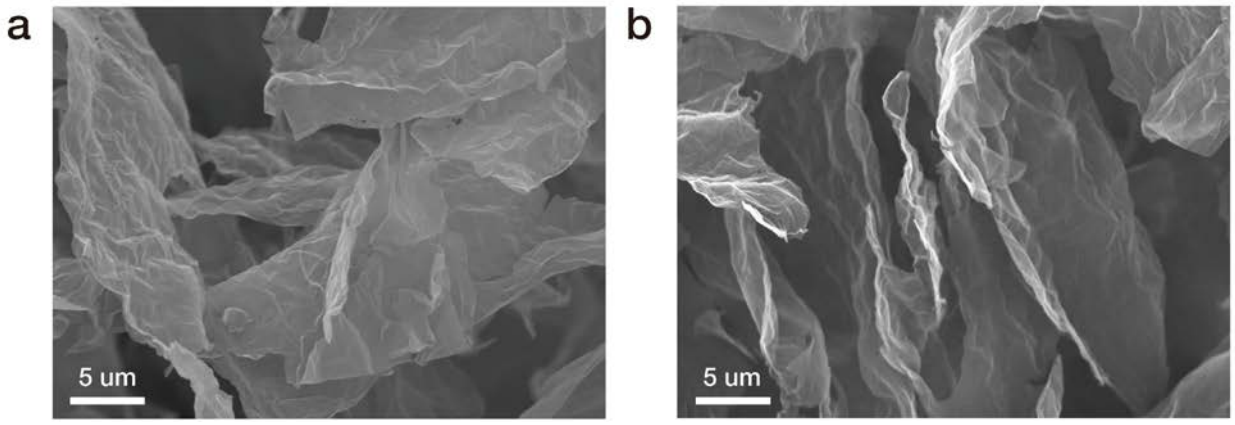

Supplementary Figure 5. SEM images of (a) Co_1-NG(O) and (b) Co_1-NG(R).

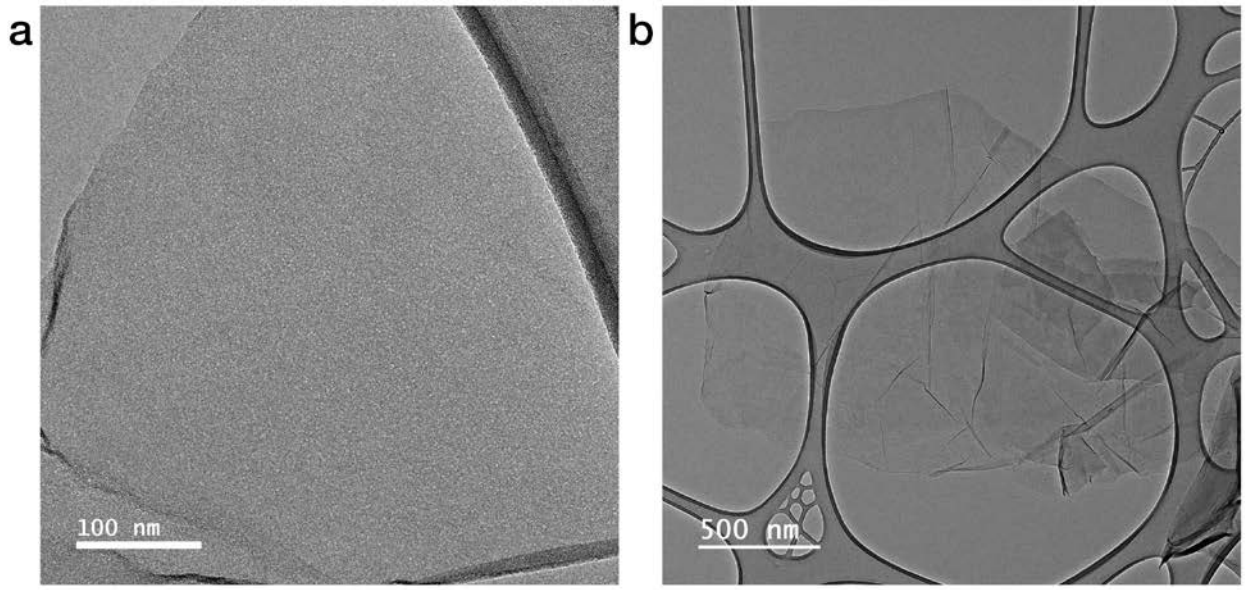

Supplementary Figure 6. TEM images of (a) Co_1-NG(O) and (b) Co_1-NG(R).

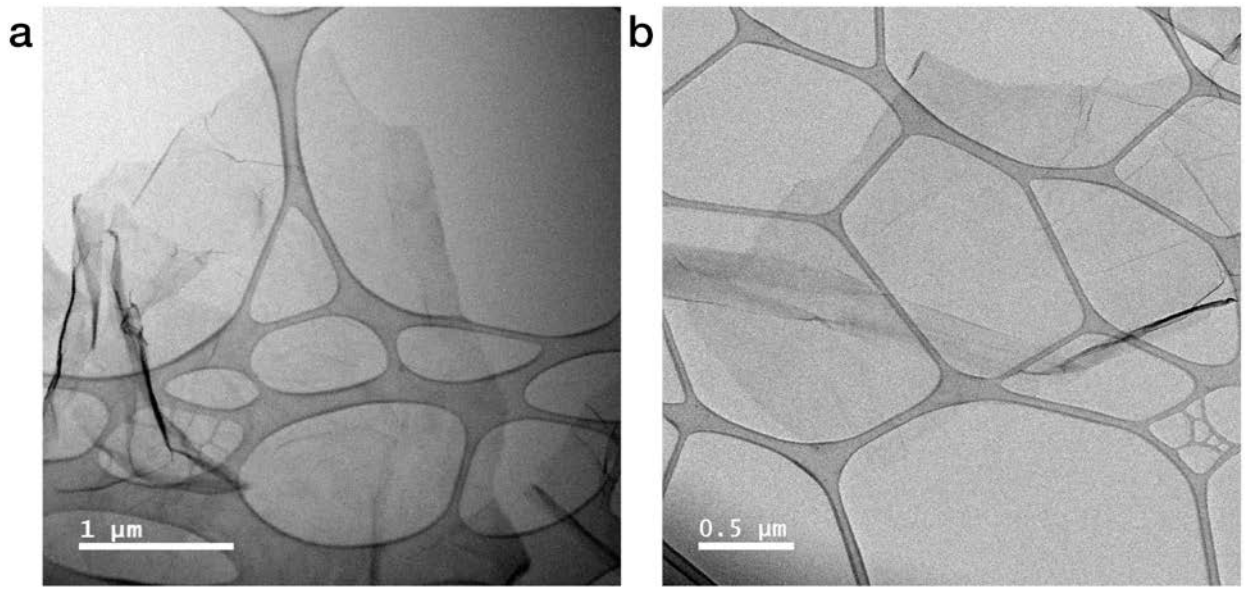

Supplementary Figure 7. STEM images of (a) Co_1-NG(O) and (b) Co_1-NG(R).

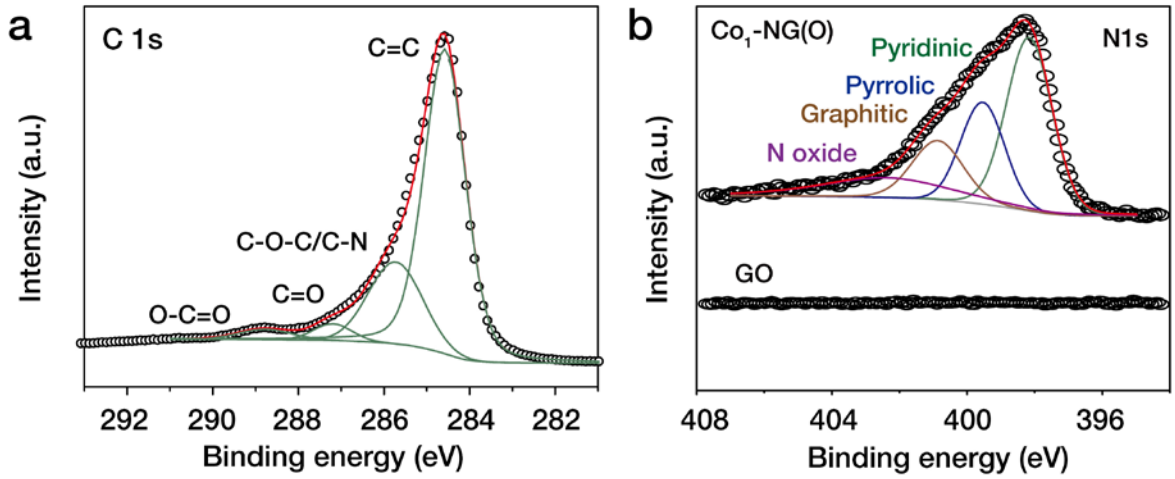

Supplementary Figure 8. Deconvoluted C 1s XPS spectra of (a) Co_1-NG(O), and N 1s XPS spectra of (b) Co_1-NG(O) and GO. The amount of nitrogen doped was 5.87 at%.

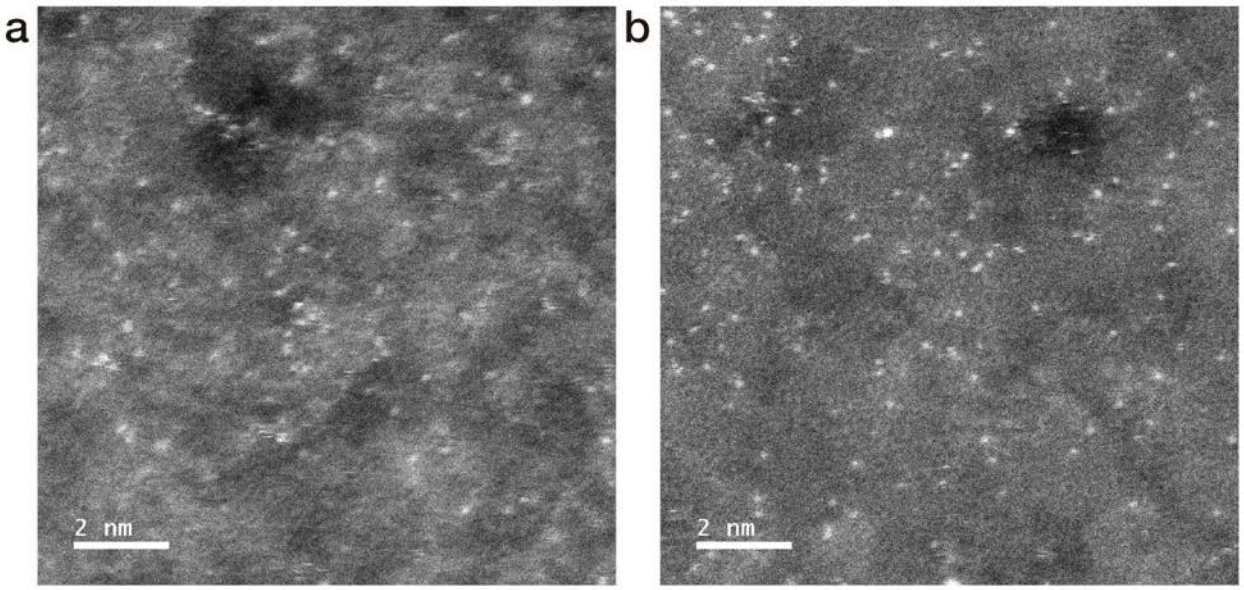

Supplementary Figure 9. High resolution HAADF-STEM images of (a) Fe_1-NG(O) and (b) Ni_1-NG(O). The bright dots represent homogeneously distributed metal atoms supported on the graphene matrix.

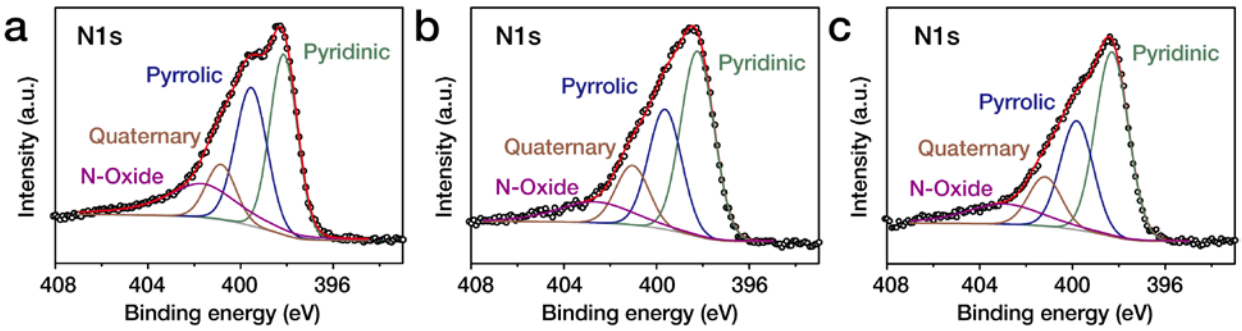

Supplementary Figure 10. Deconvoluted N 1s XPS spectra of (a) NG(O), (b) Ni_1-NG(O), and (c) Fe_1-NG(O). Distribution of pyridinic-N, pyrrolic-N, quaternary-N, and N-Oxide functional groups is shown for each catalyst.

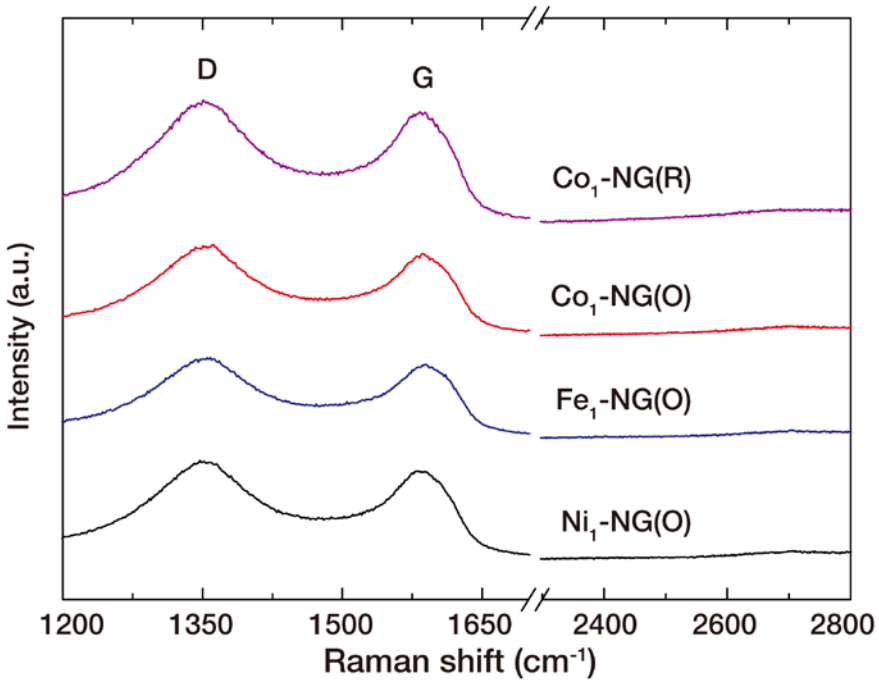

Supplementary Figure 11. Raman spectra of Co_1-NG(O), Co_1-NG(R), Fe_1-NG(O), and Ni_1-NG(O). The Raman spectra for different catalysts was obtained using 532 nm laser and 3.2% ND (neutral density) filter.

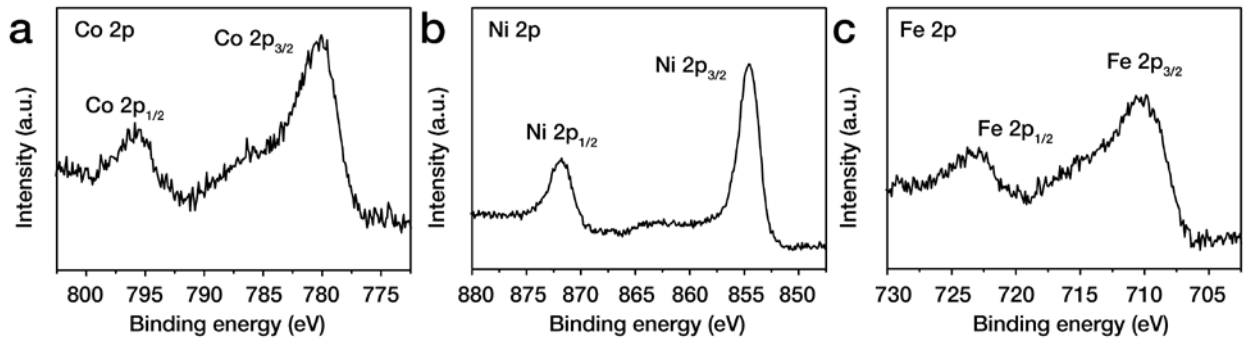

Supplementary Figure 12. (a) Co 2p XPS spectra of Co_1-NG(O), (b) Ni 2p spectra of Ni_1-NG(O), and (c) Fe 2p spectra of Fe_1-NG(O).

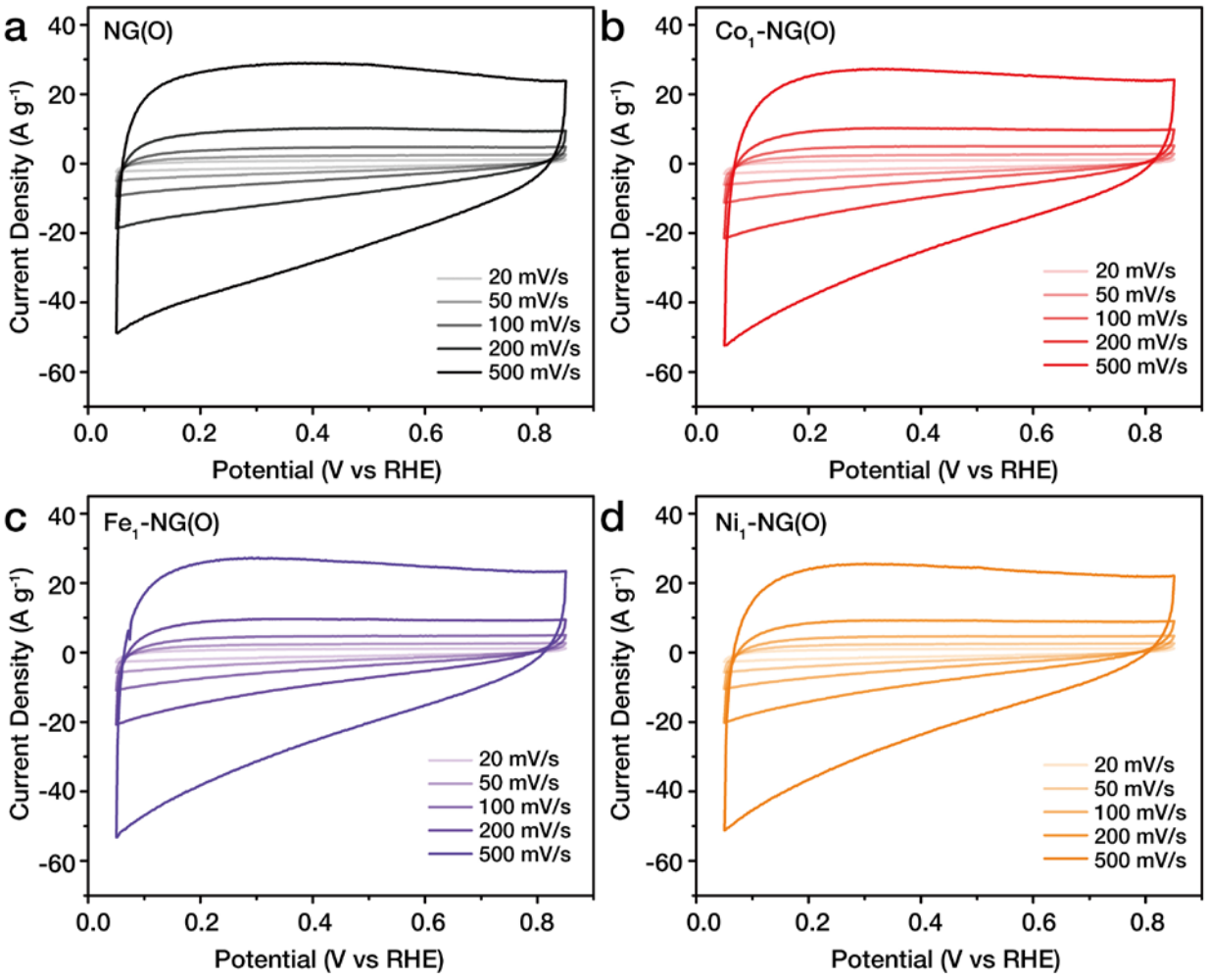

Supplementary Figure 13. Cyclic voltammetry of NG(O) and other M_1-NG(O) (M = Co, Ni and Fe) catalysts in a non-Faradaic region at different scan rates (in Ar-saturated 1 M KOH electrolyte; cell temperature of 25^{o}C).

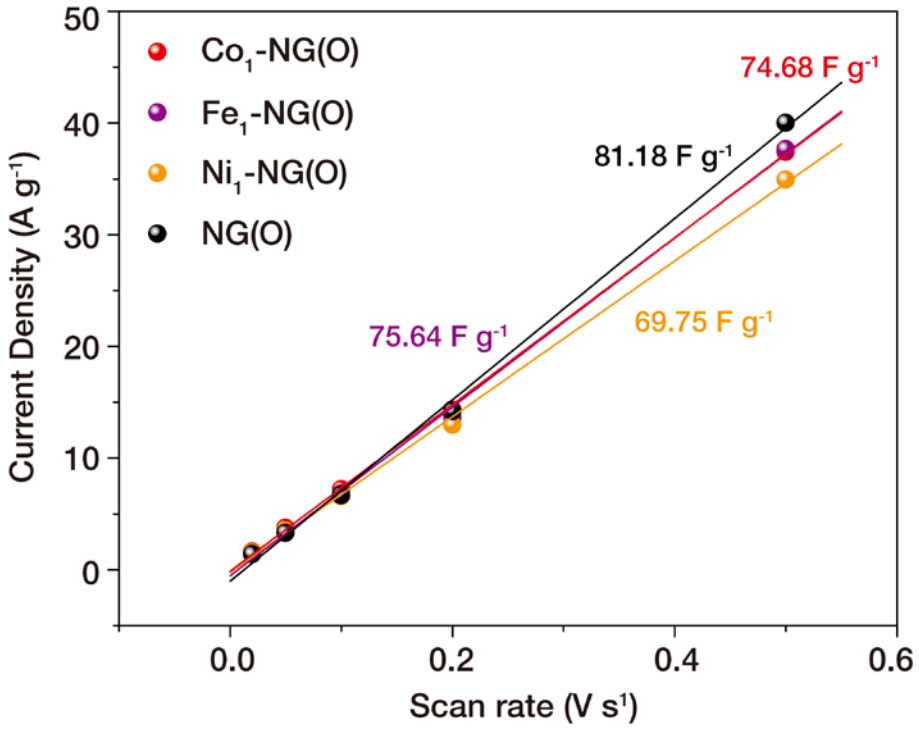

Supplementary Figure 14. Electrochemical surface area measurement of Co_1-NG(O), Fe_1-NG(O), Ni_1-NG(O), and NG(O).

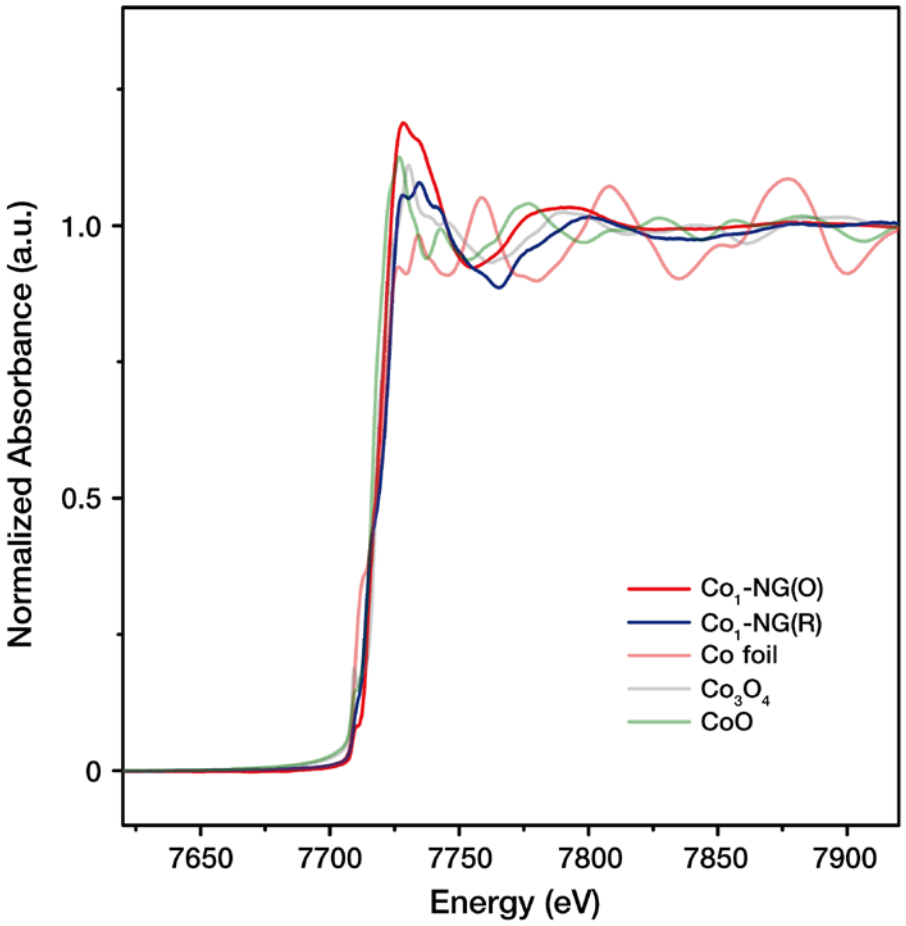

Supplementary Figure 15. XANES spectra of Co_1-NG(O), Co_1-NG(R), Co foil, Co_3O_4, and CoO.

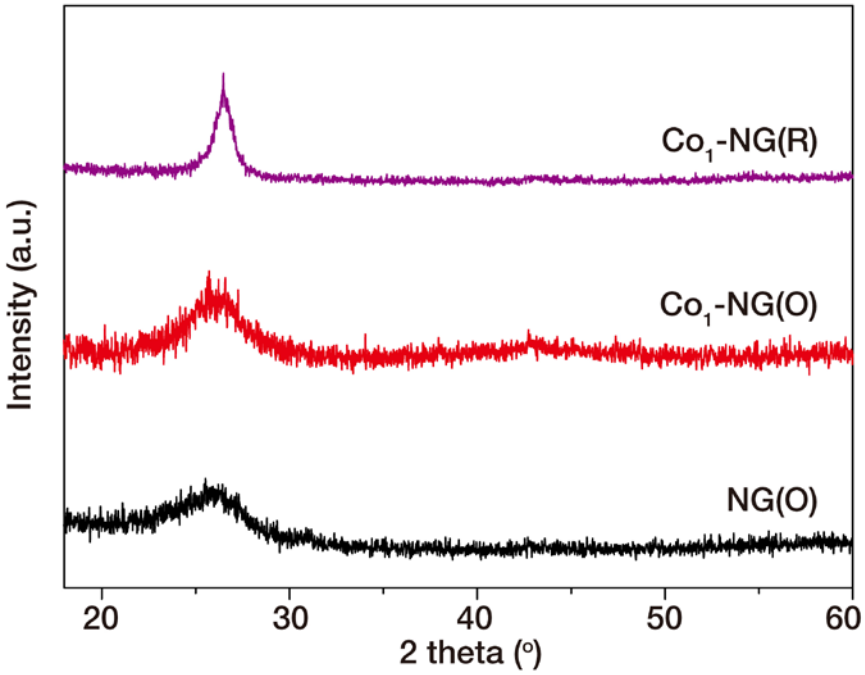

Supplementary Figure 16. XRD patterns of Co_1-NG(R), Co_1-NG(O), and NG(O). There was no metal peak observed, confirming the formation of metal atoms.

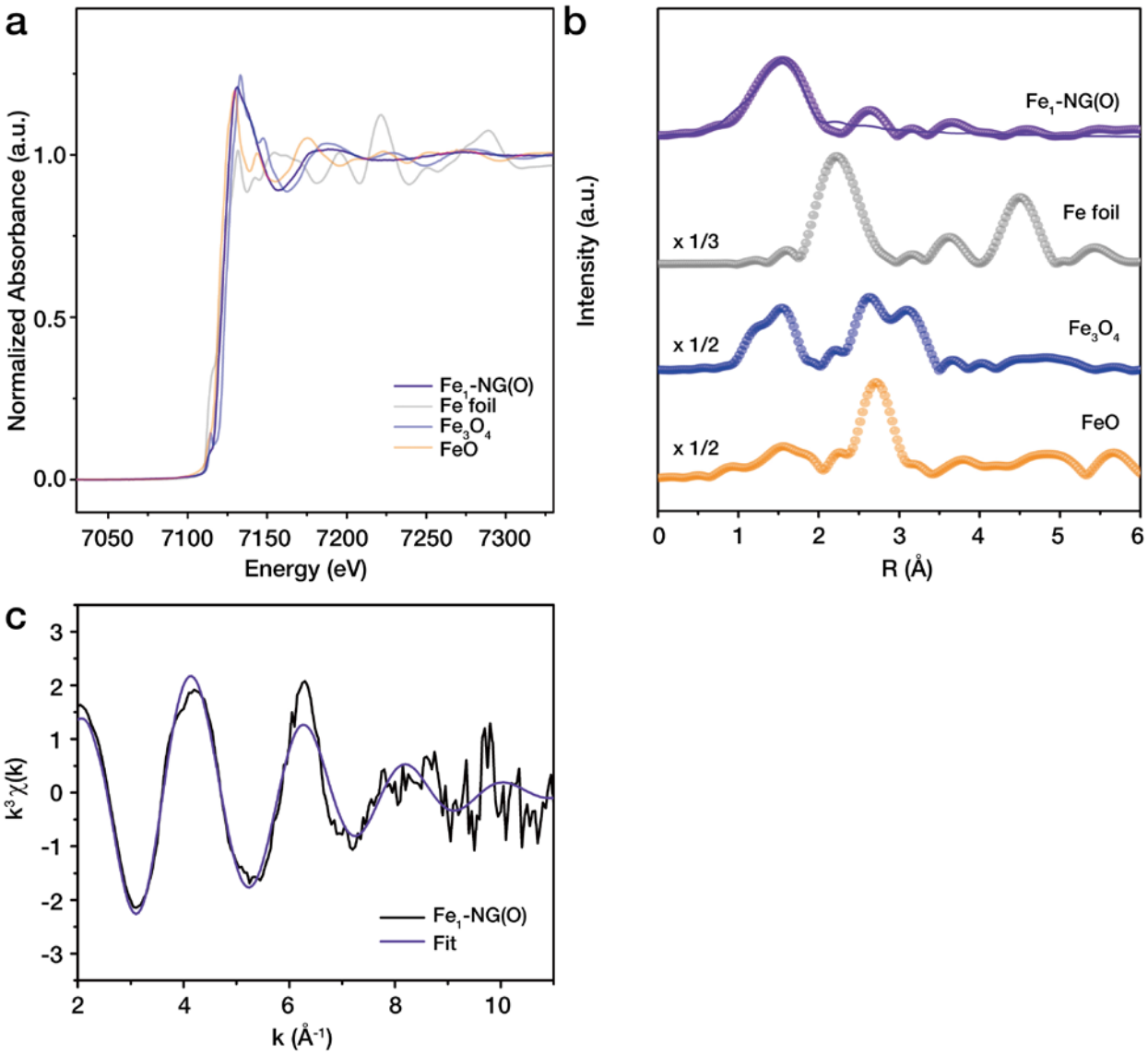

Supplementary Figure 17. XAFS measurement of Fe_1-NG (O) SAC. (**a**) XANES spectra and (**b**) Fe K-edge k^3-weighted FT-EXAFS spectra in R space for Fe_1-NG(O), Fe foil, Fe_3O_4, and FeO. (**c**) Fe K-edge EXAFS spectra in k space for Fe_1-NG(O) with the fitted result.

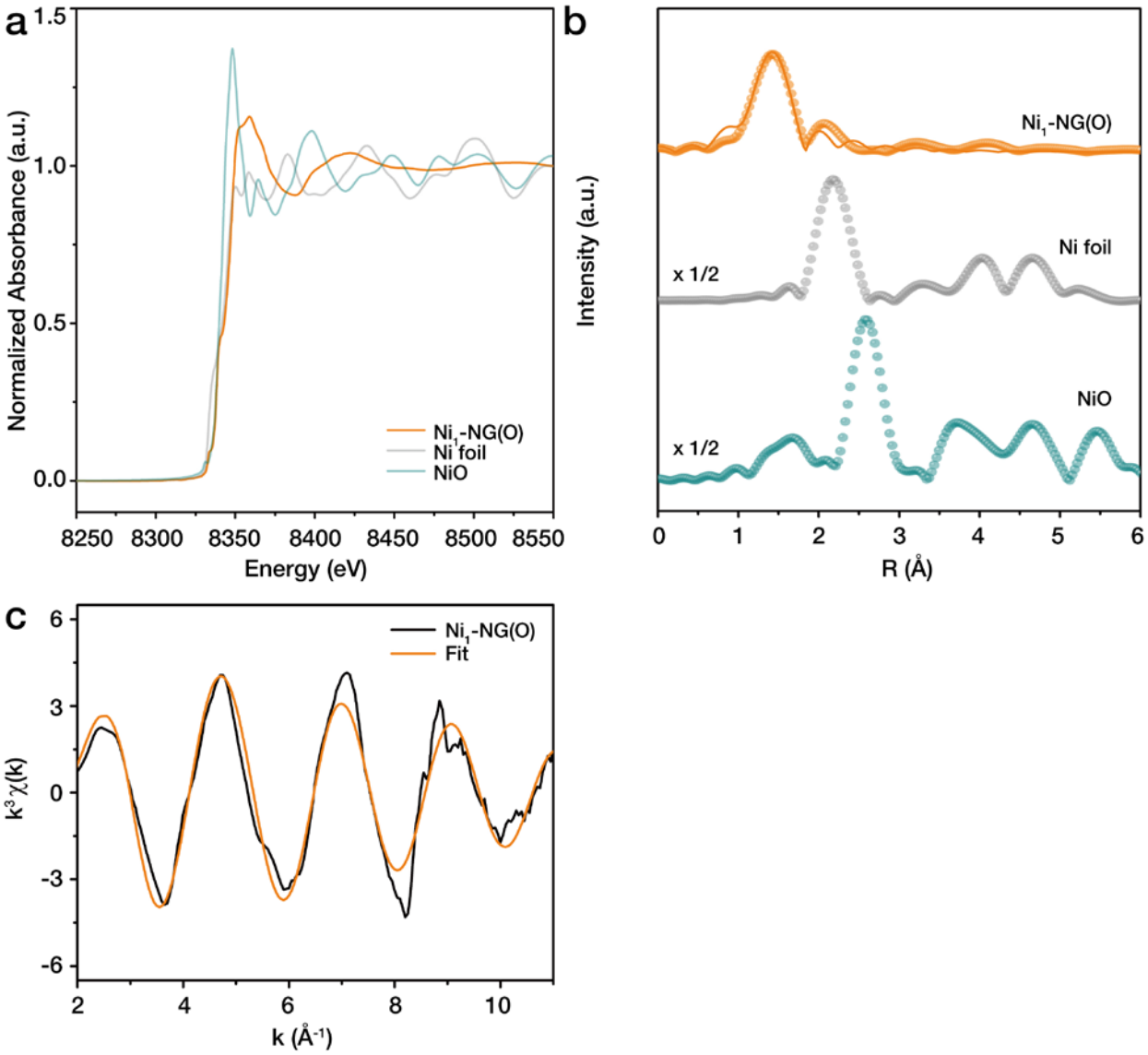

Supplementary Figure 18. XAFS measurement of Ni_1-NG (O) SAC. (**a**) XANES spectra and (**b**) Ni K-edge k^3-weighted FT-EXAFS spectra in R space for Ni_1-NG(O), Ni foil, and NiO. (**c**) Ni K-edge EXAFS spectra in k space for Ni_1-NG(O) with the fitted result.

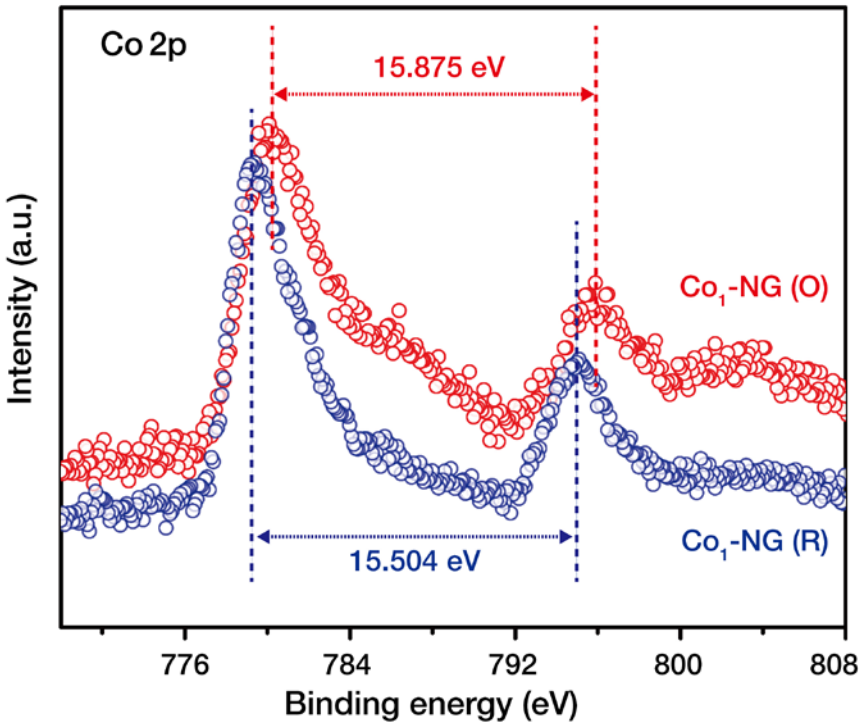

Supplementary Figure 19. Co 2p XPS spectra of Co_1-NG(O) and Co_1-NG(R). The upshift of Co 2p XPS spectra is observed and the spin-orbit splitting value (Δ_{Co} = 15.875 eV) of Co_1-NG(O) is larger than that of Co_1-NG(R) (Δ_{Co} = 15.504 eV), which indicates Co_1-NG(O) catalyst has relatively oxidized cobalt single atoms.

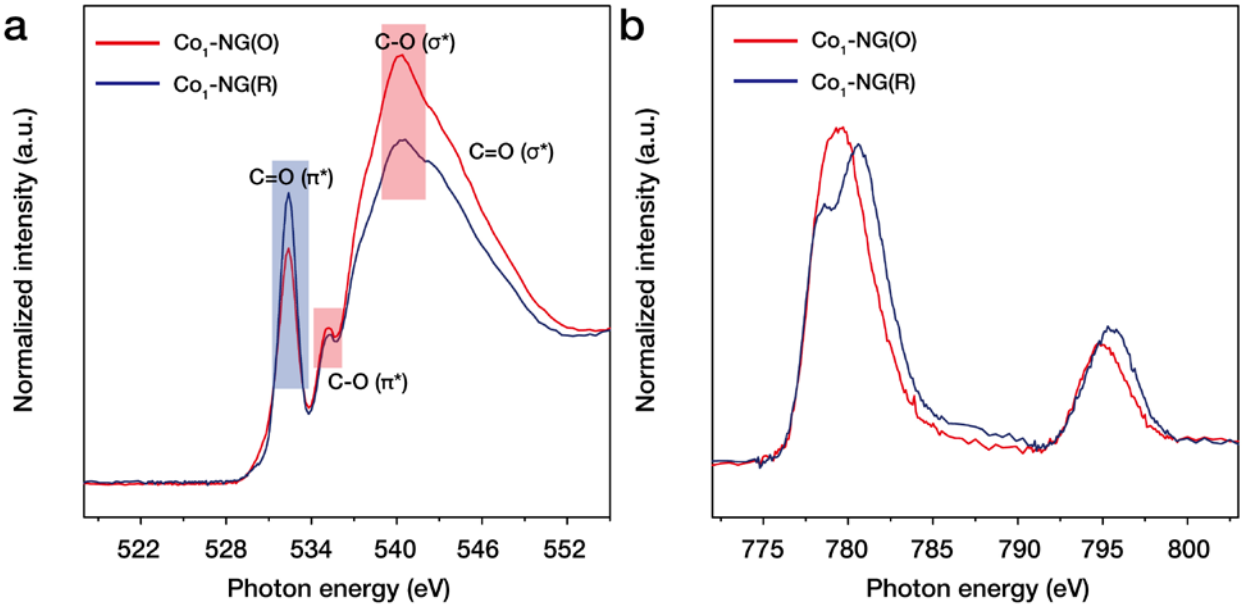

Supplementary Figure 20. (a) The oxygen K-edge and (b) cobalt L-edge NEXAFS spectra of Co_1-NG(O) and Co_1-NG(R) catalysts, measured in total electron yield (TEY) mode. The difference in the oxygen spectra is explained by the more prominent development of C-O bond (e.g. C-O-C epoxides). The downshift of cobalt L-edge spectra was observed in Co_1-NG(O), which corresponds to the enhanced unoccupied Co 3d orbitals at low energy levels. These distinctive changes resulted from the relatively electron-poor cobalt single atom centres in Co_1-NG(O), as revealed in XPS Co 2p spectra.

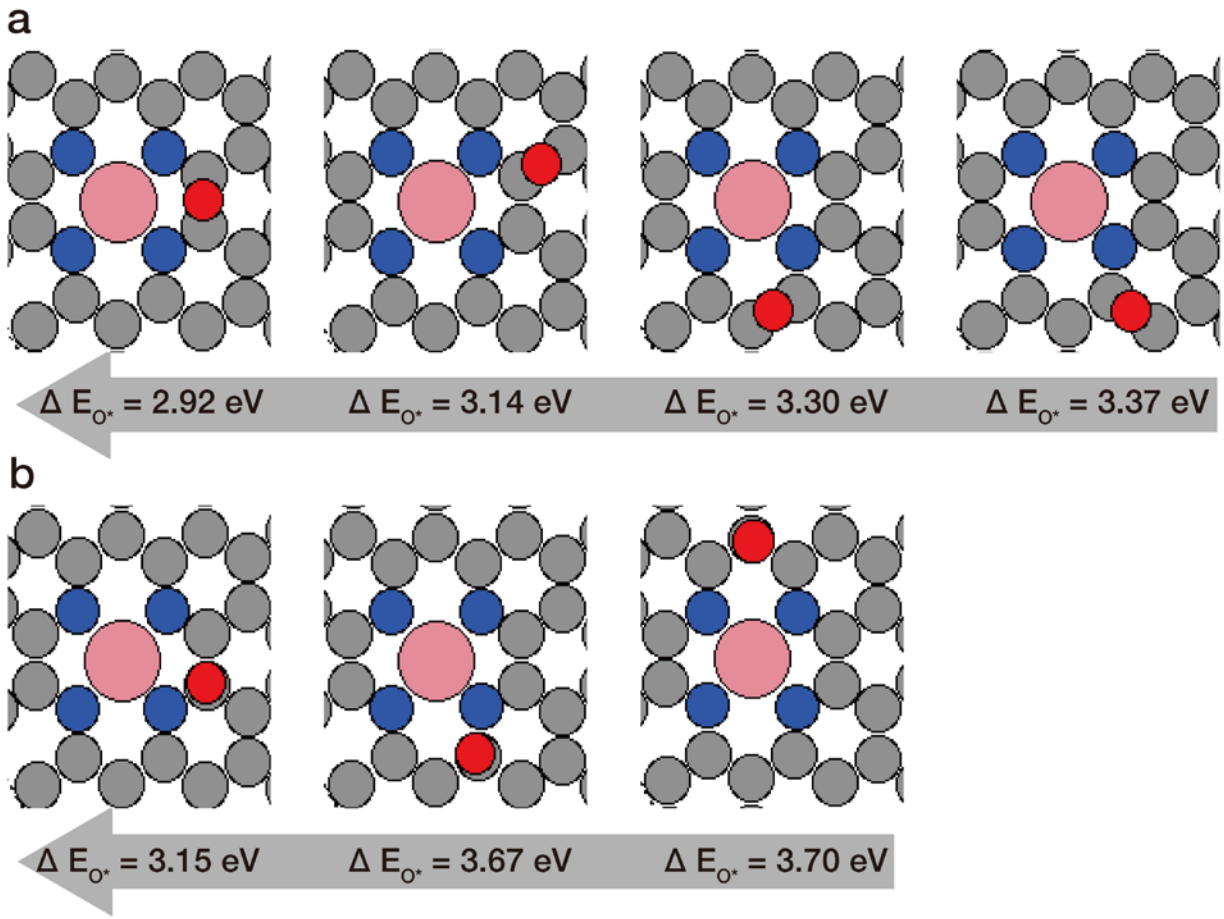

Supplementary Figure 21. Calculated oxygen adsorption energy (Δ E_{O*}) at (a) bridge and (b) on-top sites of Co-N_4/graphene.

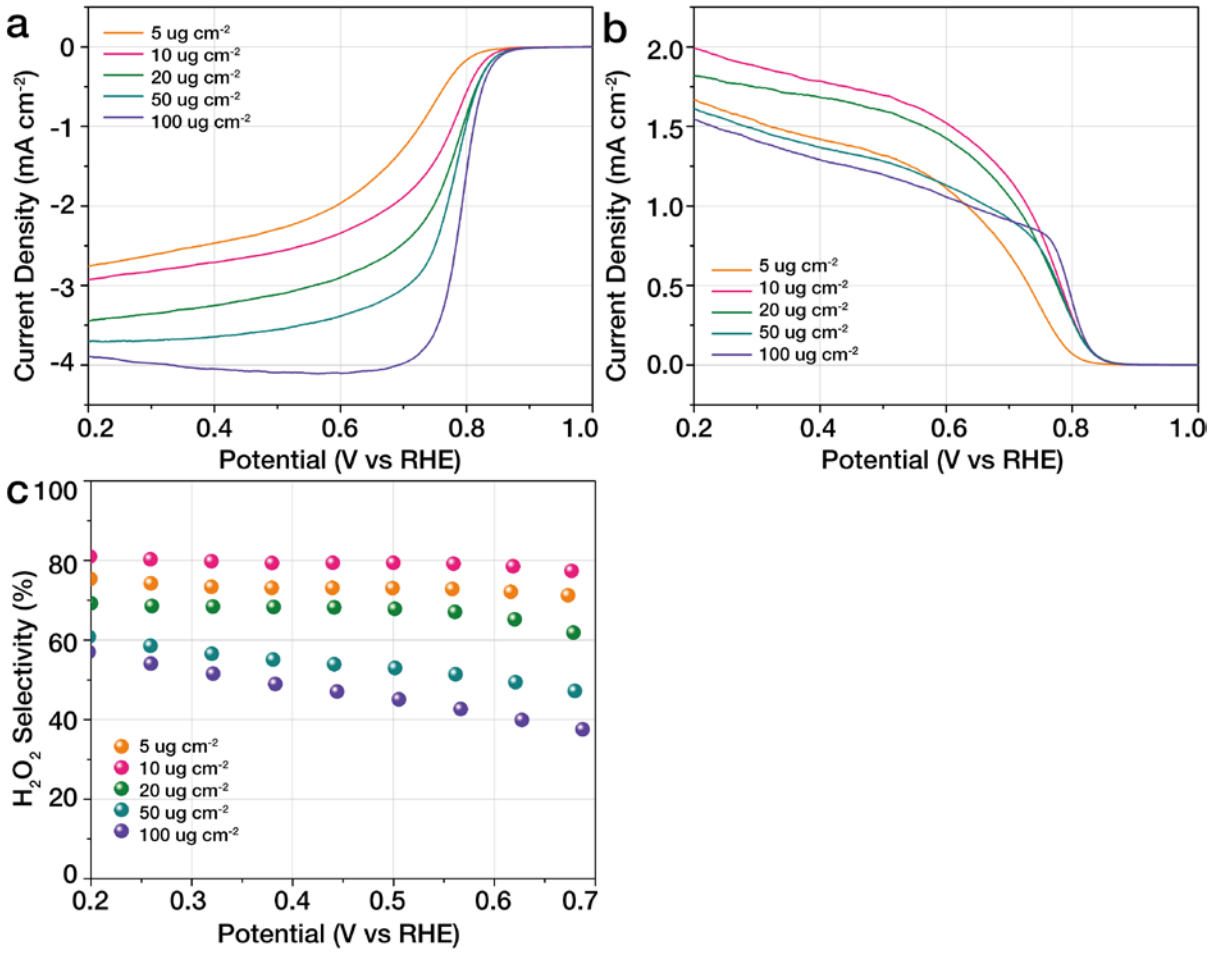

Supplementary Figure 22. The effect of catalyst loading amount on the catalytic activity and selectivity for H_2O_2 production. (a), (b) ORR polarization curves showing disk and ring current densities, (c) H_2O_2 selectivity (%) as a function of electrode potential with different loading amount of 5, 10, 20, 50, and 100 μg cm^{-2}. As the loading amount increases, the disk current density increases, and the onset potential showed slightly positive shift. However, the ring current density decreases as the catalyst loading amount increases, resulting in the reduction of H_2O_2 selectivity while increasing the loading amount. As the catalyst layer becomes thicker, diffusion pathways are increased and the reaction intermediates are more likely to be trapped inside the catalyst layer leading to the consecutive electroreduction to H_2O. Therefore, the catalyst loading amount is one of the significant factors and the optimal loading amount may depend on the morphology of the catalyst (e.g. sheets or spherical particles). The optimized catalyst loading amount of our Co_1-NG(O) catalyst was 10 μg cm^{-2} and this value was fixed for all the related electrochemical tests.

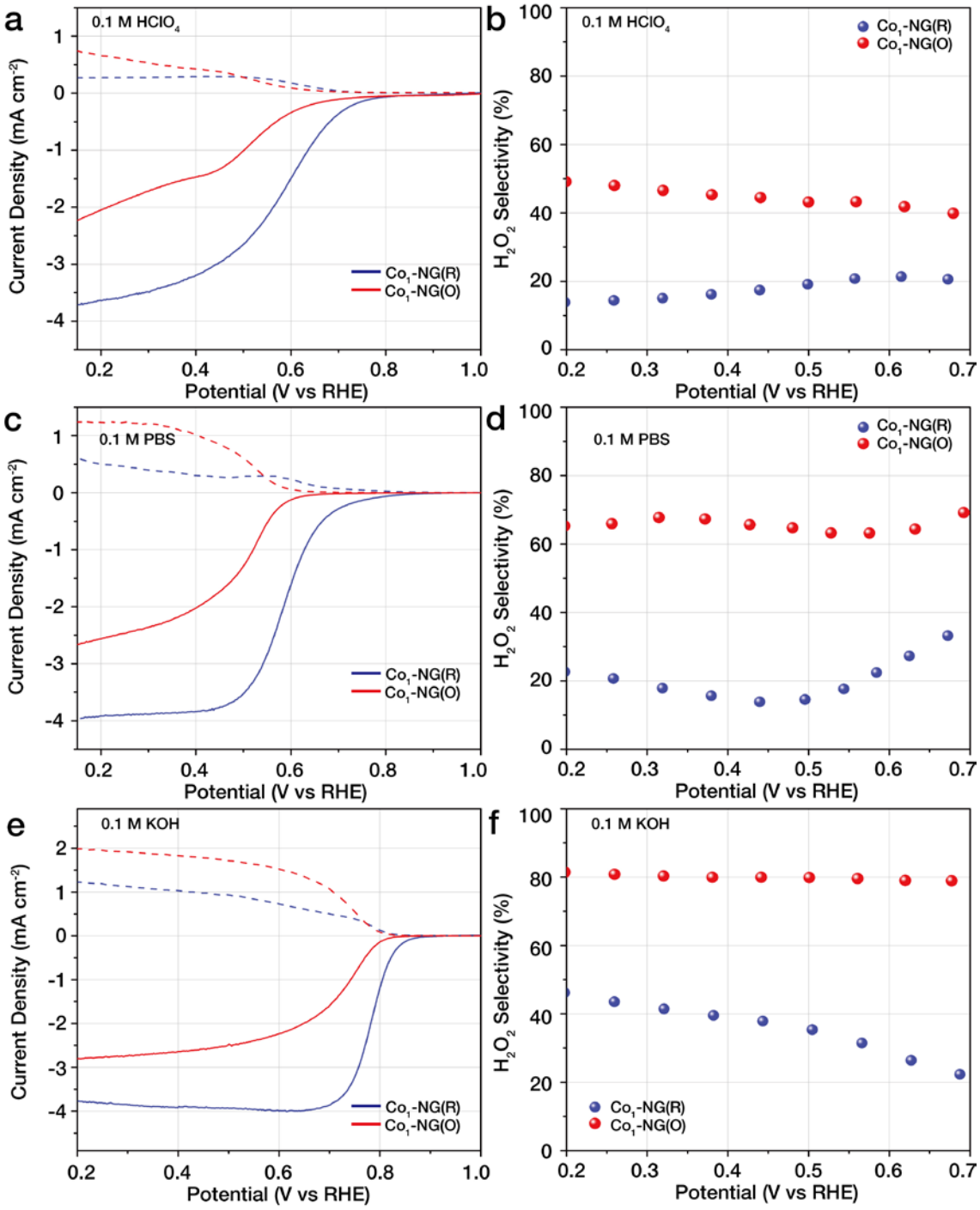

Supplementary Figure 23. ORR polarization curves and H_2O_2 selectivity of Co_1-NG(O) and Co_1-NG(R) in three different electrolytes (acidic: 0.1 M $HClO_4$, neutral: 0.1 M phosphate, and basic: 0.1 M KOH).

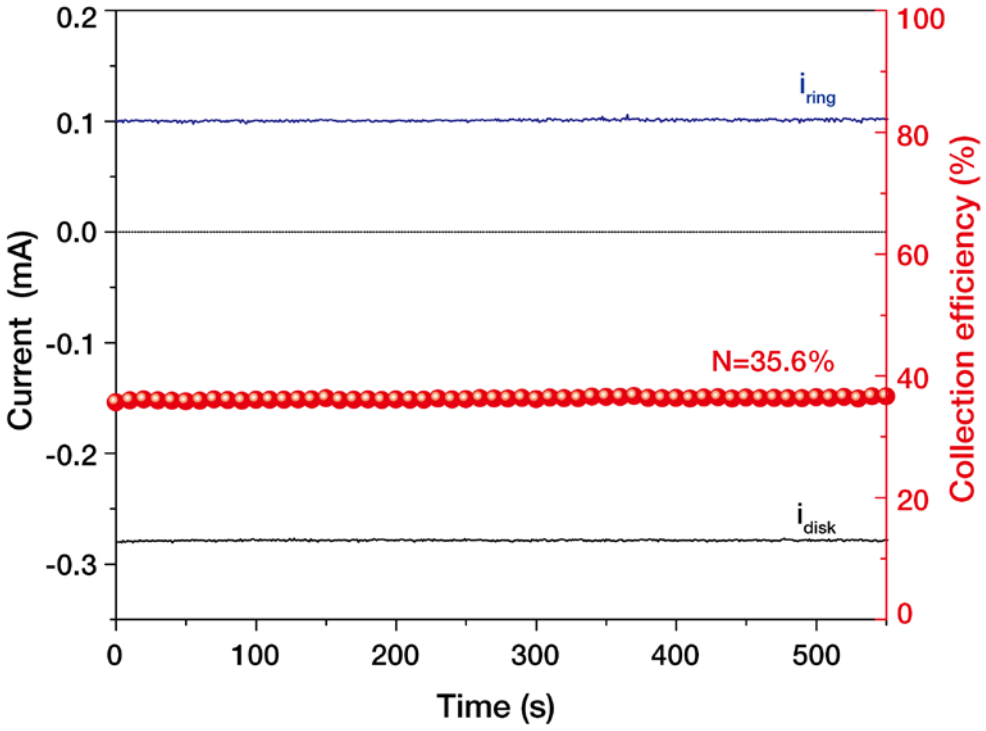

Supplementary Figure 24. Derivation of the collection efficiency (N) of the rotating ring-disk electrode. The RRDE was placed in a 0.1 M KOH electrolyte solution containing a small concentration (~2 mM) of $K_3Fe(CN)_6$. At the disk electrode, the potential of -0.3 V (vs. Ag/AgCl) was applied with rotation rate of 1,600 rpm.

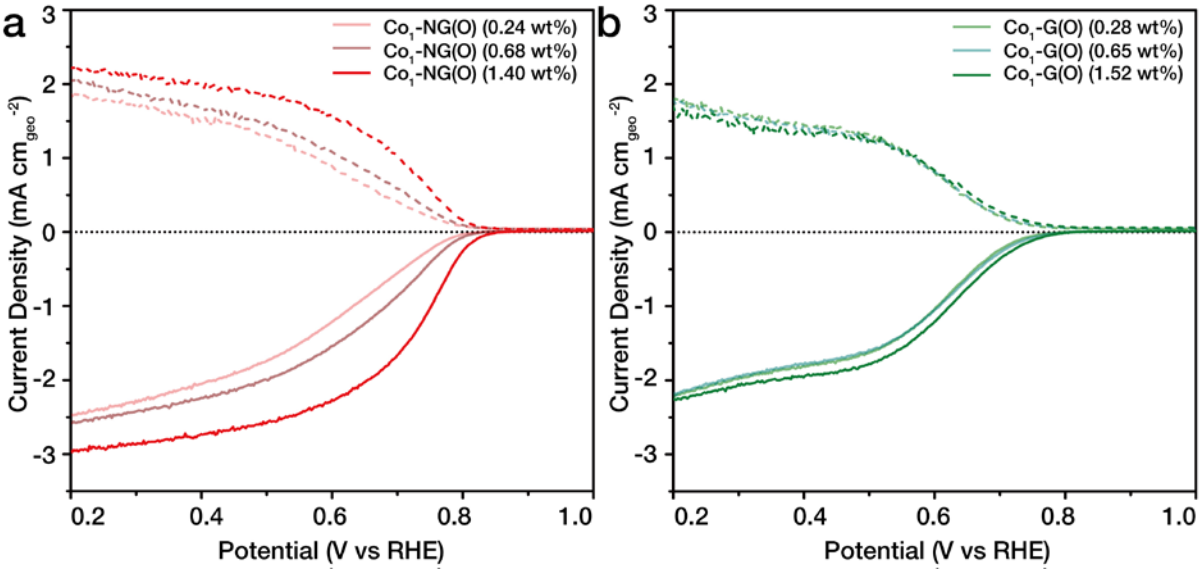

Supplementary Figure 25. ORR polarization curves in alkaline media (0.1 M KOH) for (a) Co_1-NG(O) and (b) Co_1-G(O) with various Co (wt%) amounts.

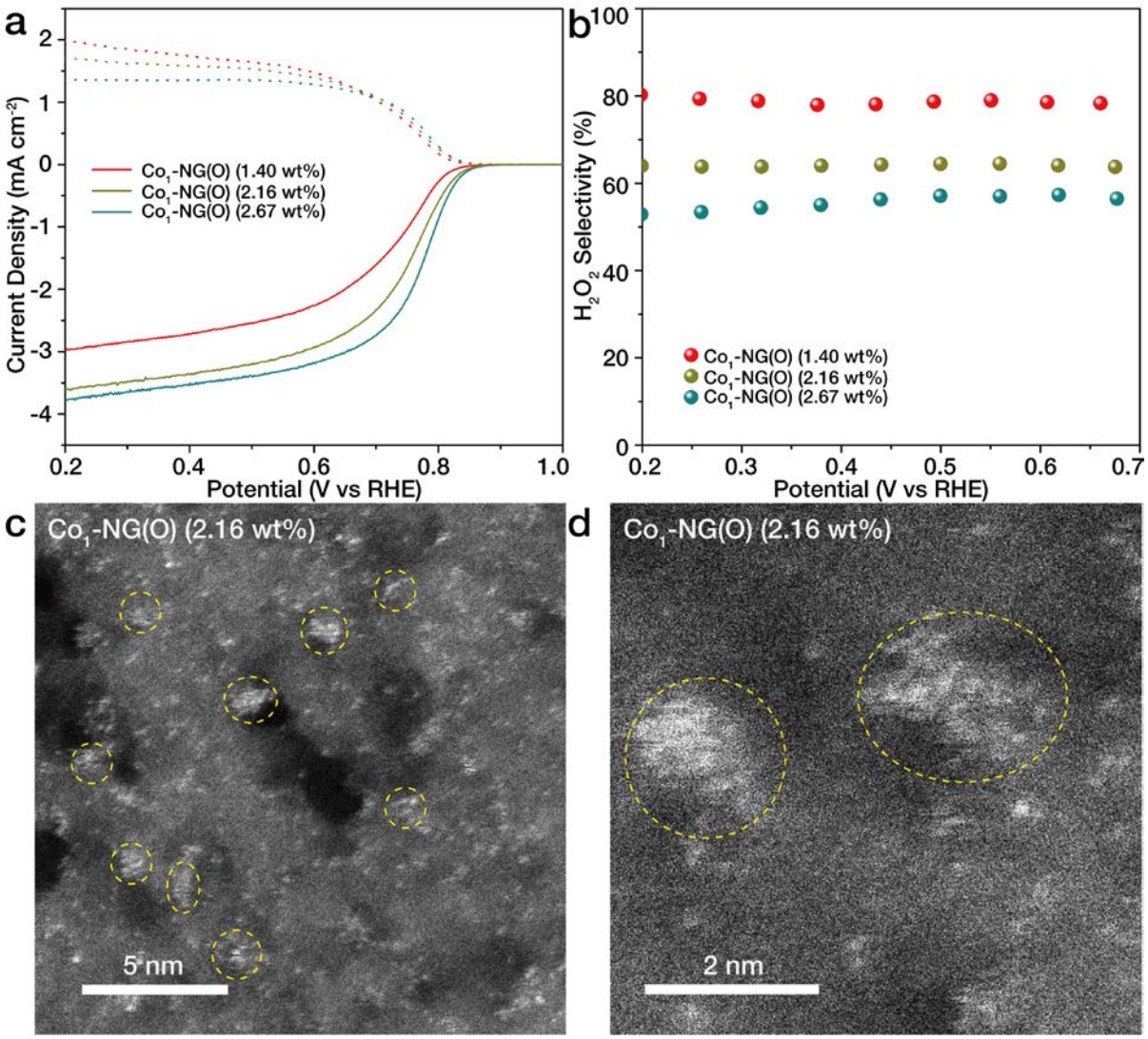

Supplementary Figure 26. (a) ORR polarization curves and (b) H_2O_2 selectivity for Co_1-NG(O) catalysts with Co amounts of 1.40, 2.16, and 2.67 wt% in alkaline media. (c), (d) HAADF-STEM images of Co_1-NG(O) (2.16 wt%). As the cobalt amount increased, cobalt atoms agglomerated and nanoclusters formed resulting in the reduction of the electrochemical H_2O_2 production performance (ring current and H_2O_2 selectivity decreased for catalysts with 2.16 and 2.67 wt% Co).

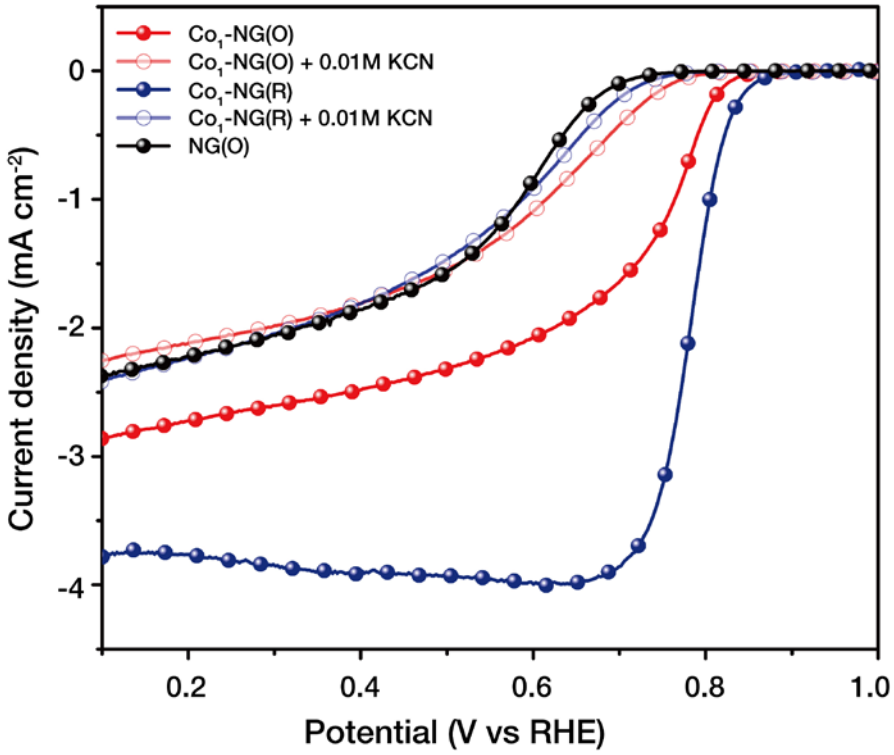

Supplementary Figure 27. ORR polarization curves in alkaline media (0.1 M KOH) for Co_1-NG(O), Co_1-NG(O) + 0.01 M KCN, Co_1-NG(R), Co_1-NG(R) + 0.01 M KCN, and NG(O). Cobalt metal atoms were poisoned by KCN to verify the catalytically active sites for H_2O_2 production.

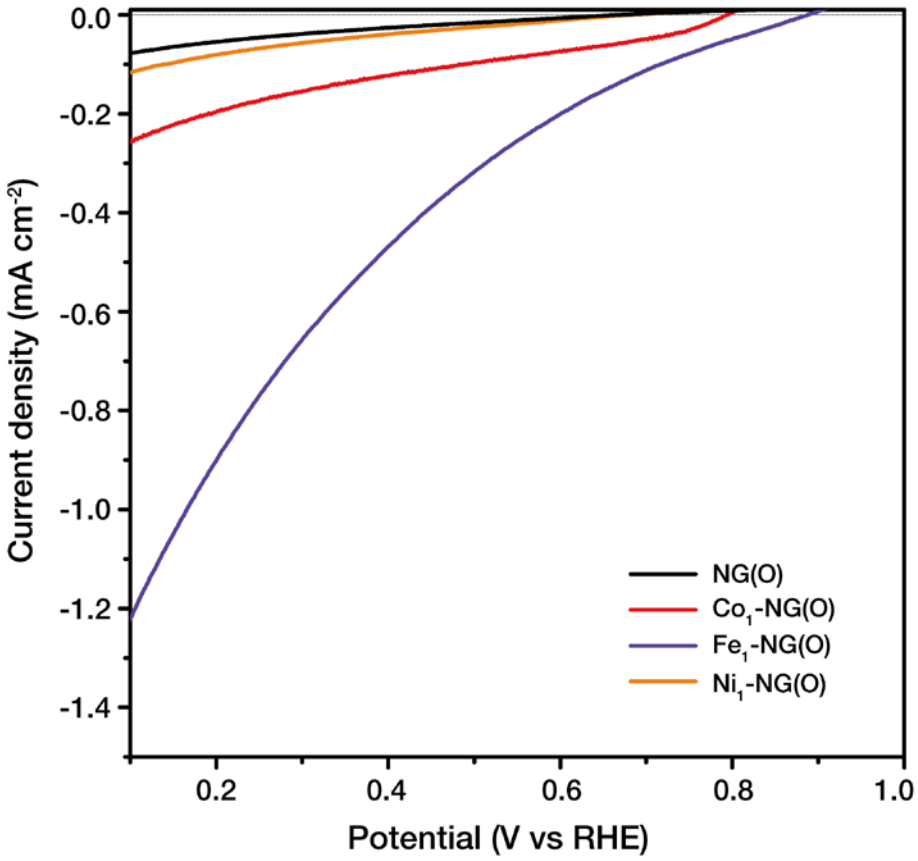

Supplementary Figure 28. Peroxide reduction reaction (PRR) for NG(O), Co_1-NG(O), Fe_1-NG(O), and Ni_1-NG(O) (1,600 rpm and 10 μg cm^{-2} in 0.1 M KOH electrolyte, containing 3.5 mM H_2O_2). Various metal single atom sites may be necessary to catalyze the multi-electronic ORR, which may proceed through a direct $4e^-$ pathway or indirect $2e^-$ pathways involving H_2O_2 intermediates. Further electroreduction of H_2O_2 to H_2O at the active site is not desirable for the efficient production of H_2O_2 and therefore PRR (H_2O_2 → H_2O) catalysis should be suppressed.

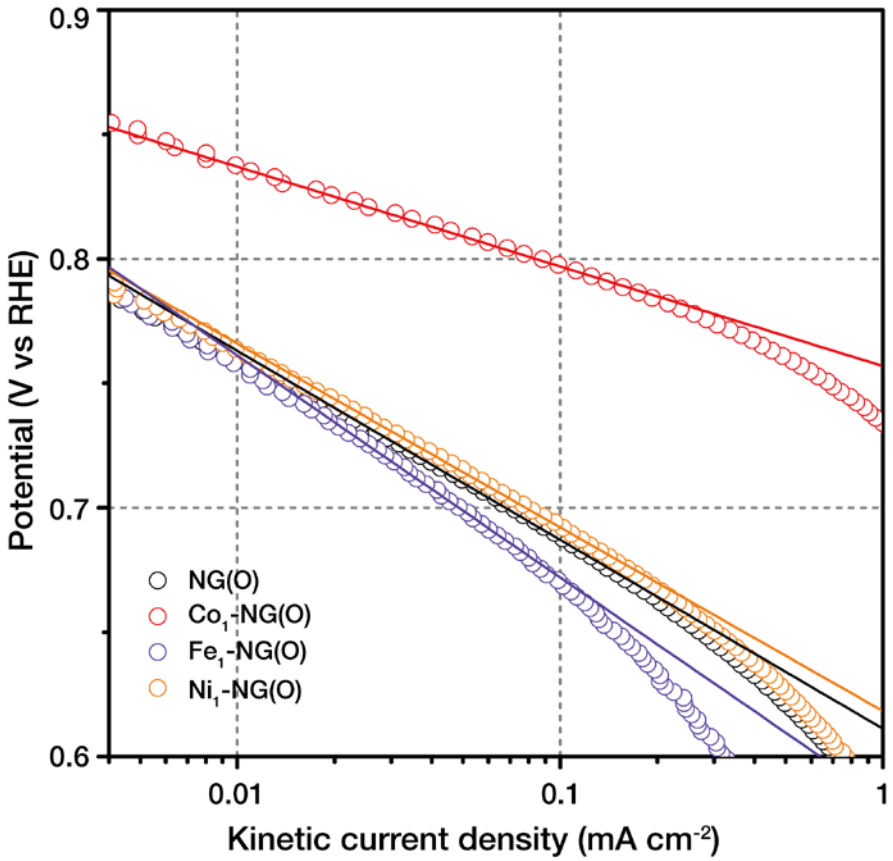

Supplementary Figure 29. Tafel plots of NG(O), Co_1-NG(O), Fe_1-NG(O), and Ni_1-NG(O) comparing their activity for H_2O_2 production. Kinetic current density was calculated from the current density of the ring electrode.

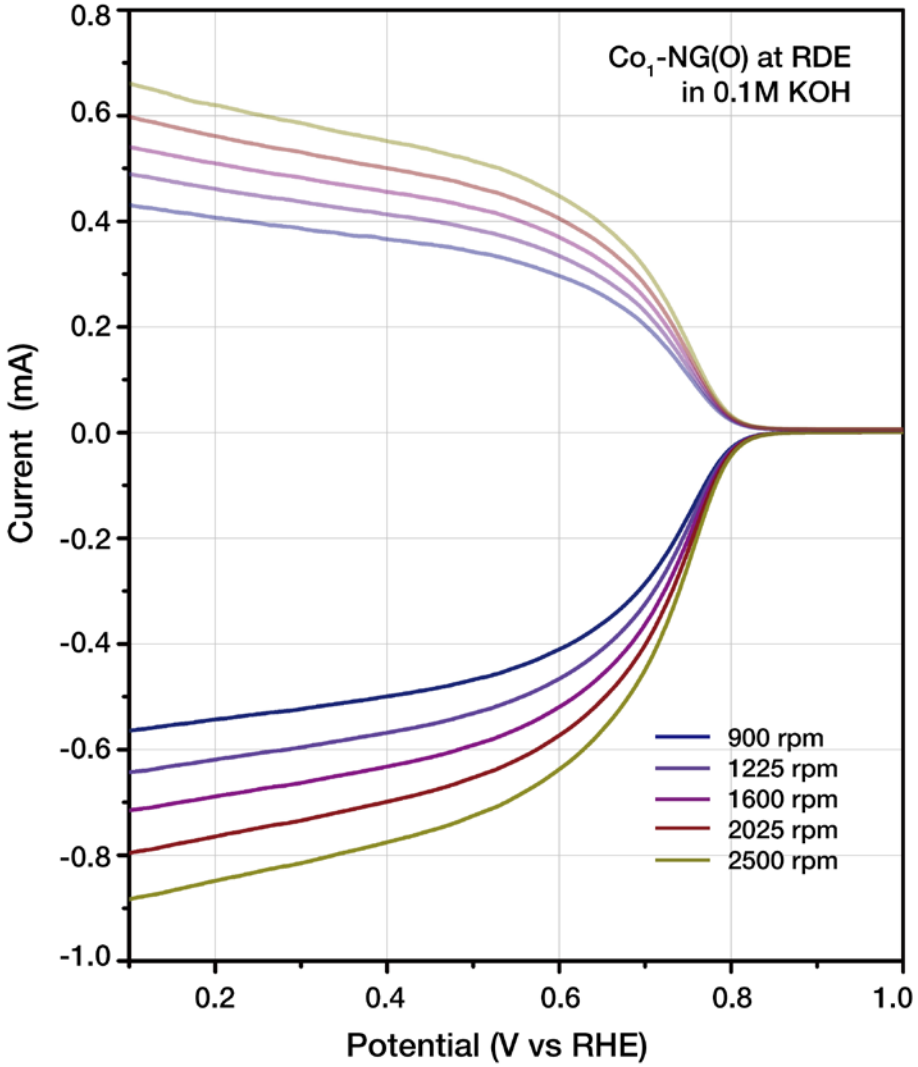

Supplementary Figure 30. RRDE polarization curves of Co_1-NG(O) catalyst under different rotation rates (ω = 900, 1225, 1600, 2025, 2500 rpm).

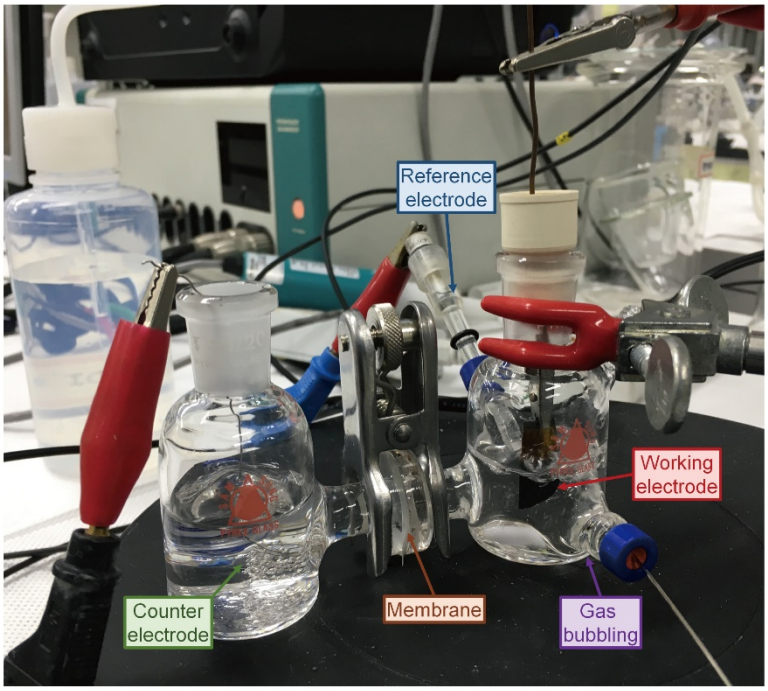

Supplementary Figure 31. Custom-made electrochemical H-type cell.

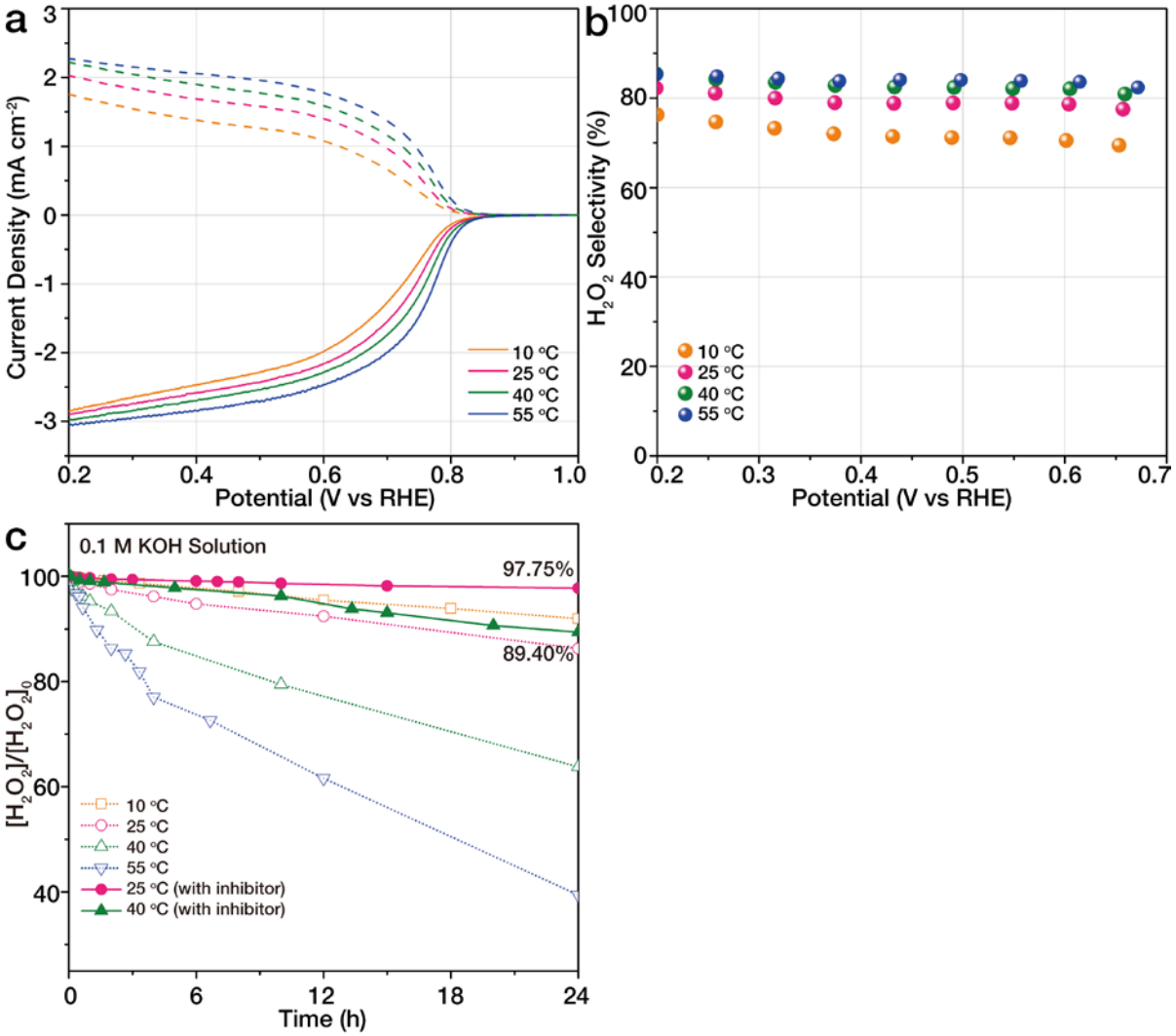

Supplementary Figure 32. Effect of reaction temperature on the kinetics of ORR activity and decomposition of H_2O_2. (a) RRDE polarization curves, (b) H_2O_2 selectivity (%), and (c) H_2O_2 decomposition rate of Co_1-NG(O) in 0.1 M KOH at 10 (yellow), 25 (pink), 40 (green), and 55 ^oC (blue). As the reaction temperature increases, the ORR currents increase while the produced H_2O_2 is decomposed more rapidly. After 1 day in 0.1 M KOH solution, about 60 % of the initial amount of peroxide (0.3 wt%) disappeared at 55 ^oC without any inhibitor. When the inhibitor (10 mM of EDTA) was added at 25 ^oC and 40 ^oC, the peroxide decomposition rate was significantly reduced. 97.75% of peroxide was stable for 1 day at 25 ^oC with the inhibitor, showing the optimal condition for our setup.

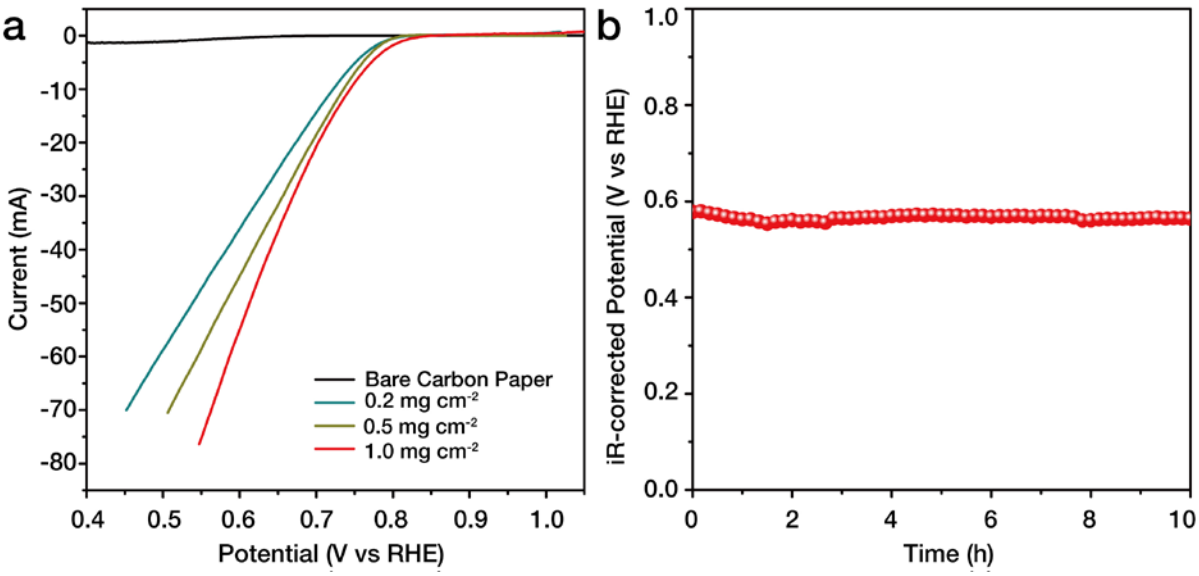

Supplementary Figure 33. O_2 reduction results obtained on the carbon paper electrode loaded with Co_1-NG(O) in O_2-saturated 0.1 M KOH electrolyte. (**a**) IR-corrected polarization curves as a function of catalyst loading weight. A slightly positive shift of onset potential and enhanced current density are resulted from the increased amount of active site on the electrode layer (electrode surface area was 1 cm^2). (**b**) V-t curve under a constant current of 50 mA for producing H_2O_2 in the H-type cell (catalyst loading: ~ 1.0 mg cm^{-2}).

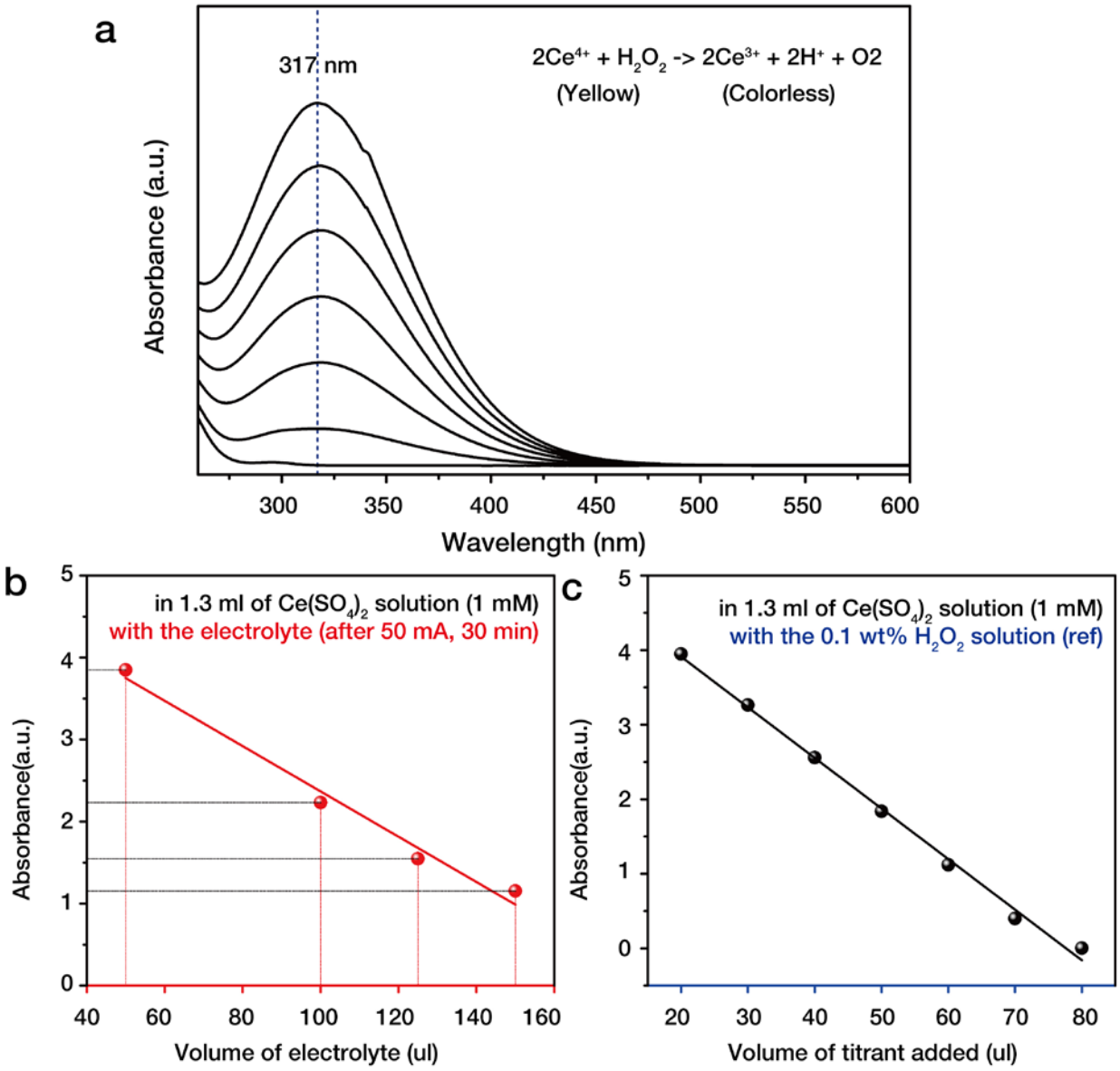

Supplementary Figure 34. The H_2O_2 concentrations in electrolytes were measured by titration using standard ceric sulfate solution, $Ce(SO_4)_2$. (**a**) UV-Visible spectra of cerium titration solution with the gradual addition of the electrolyte after H_2O_2 production or 0.1 wt% H_2O_2 solution (control group with the known concentration) were obtained. (**b**, **c**) The linear calibration curves between absorbance and the volume of electrolyte (or titrant, 0.1 wt% H_2O_2 solution) added.

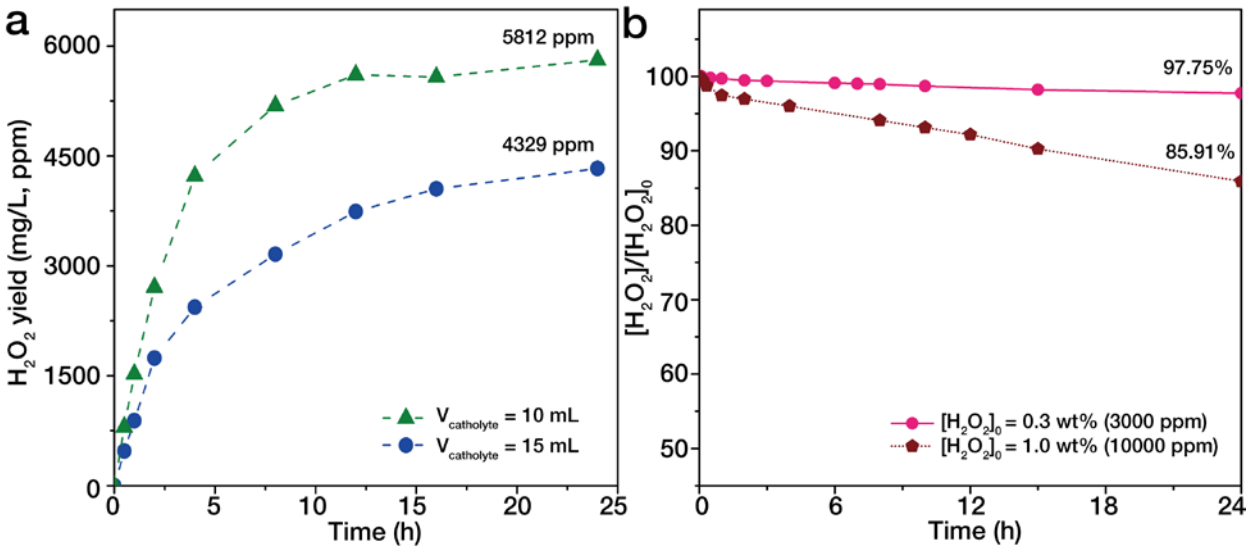

Supplementary Figure 35. (a) Accumulation of H_2O_2 over time in our custom-made H-type cell (under a constant current of 50 mA). H_2O_2 concentration also depends on the initial volume of electrolyte ($V_{catholyte}$ = 10 or 15 mL). Previously, several cell designs for the electrochemical production of H_2O_2 have been proposed and they used small-scale reactors containing a small volume (e.g. 0.5 mL) of electrolyte (ref. 9). However, the accumulated concentration of H_2O_2 can be easily decreased by the further reduction of H_2O_2 to H_2O or a chemical decomposition to O_2. **(b) Stability test to investigate the effect of the initial H_2O_2 concentration (0.3, 1.0 wt%).** Our result reveals that H_2O_2 molecules are more easily decomposed as the initial H_2O_2 increases. This issue might be resolved by employing a new type of cell such as flow cell which can hinder the accumulation of H_2O_2, thus improving the current efficiency. With further improvement in storage techniques of H_2O_2 in the years ahead, we expect that our Co_1-NG(O) can show more enhanced H_2O_2 storage performance.

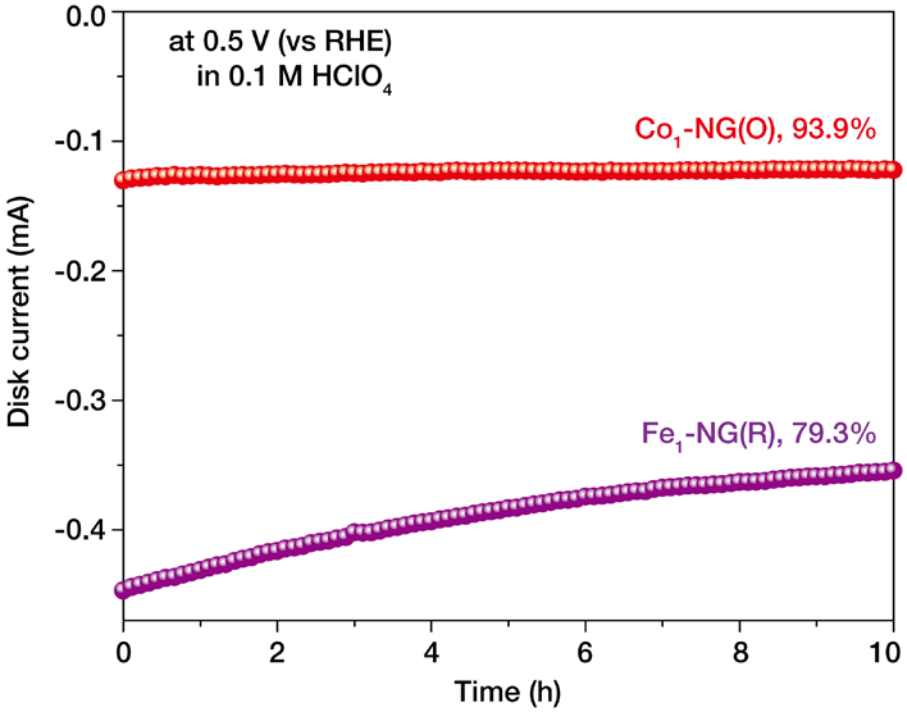

Supplementary Figure 36. Long-term durability test at constant potentials of 0.5 V (versus RHE) for 10 h in O_2-saturated 0.1 M $HClO_4$ to examine the stability of catalysts in acidic media. Our Co_1-NG(O) catalyst retains ~ 94% of its initial current after 10 h in acidic media, but the iron-based catalyst, Fe_1-NG(R), showed a worse retention (~79%).

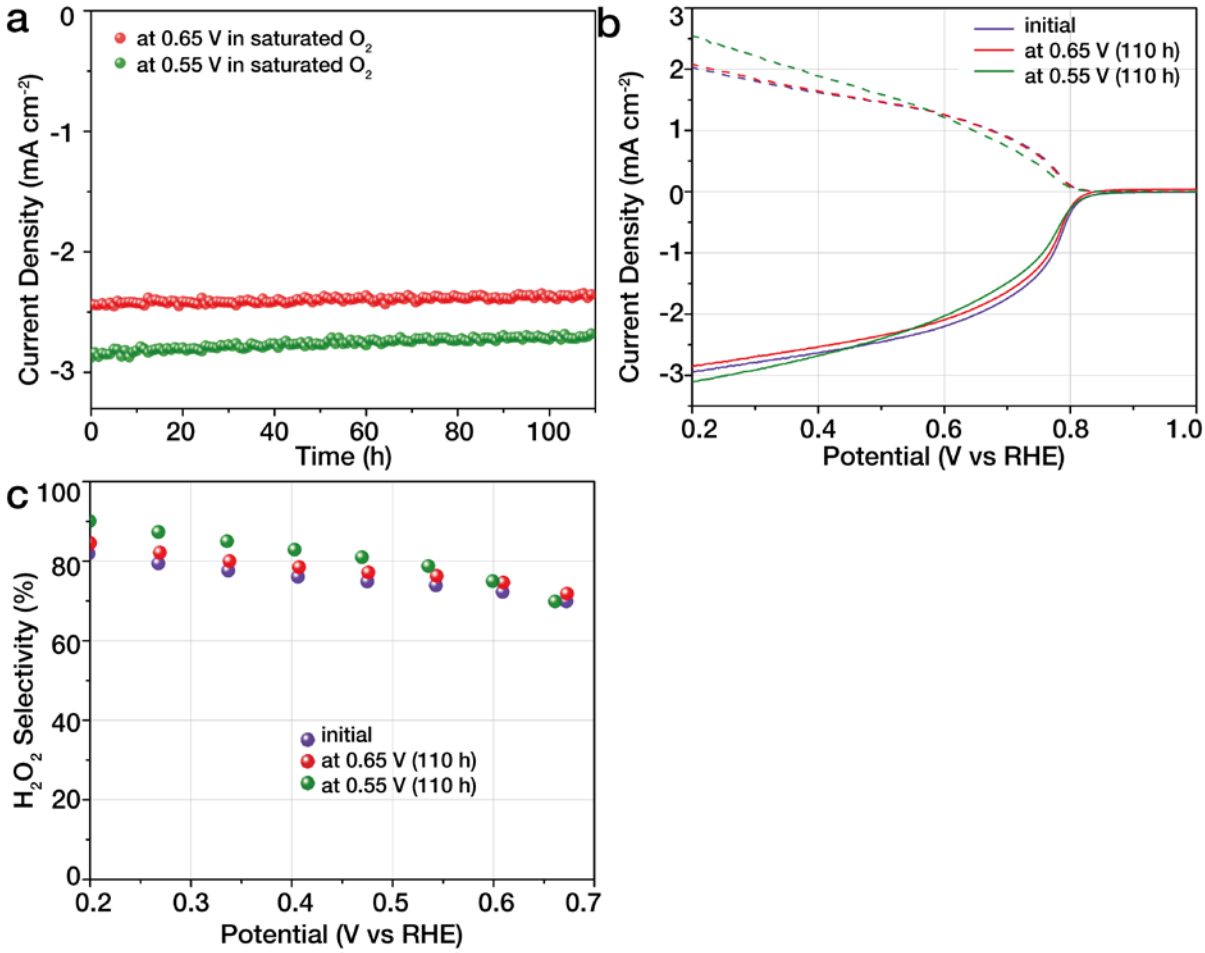

Supplementary Figure 37. (a) Chronoamperometry stability test of Co_1-NG(O) at 0.65 and 0.55 V in 0.1 M KOH electrolyte with RRDE setup. (b), (c) ORR polarization curves and H_2O_2 selectivity of catalysts after stability tests (the electrolyte was replaced with new KOH solution before conducting ORR analysis). Our Co_1-NG(O) catalyst maintains its ORR performance even after 110 h (at 0.65V and 0.55 V). At 0.55 V, the disk and ring current slightly decreased near the onset potential range (0.7-0.8 V vs. RHE) whereas they increased in the high overpotential range (0.2-0.5 V). Thus, Co_1-NG(O) can retain its high selectivity towards H_2O_2 even after the 110 h durability test.

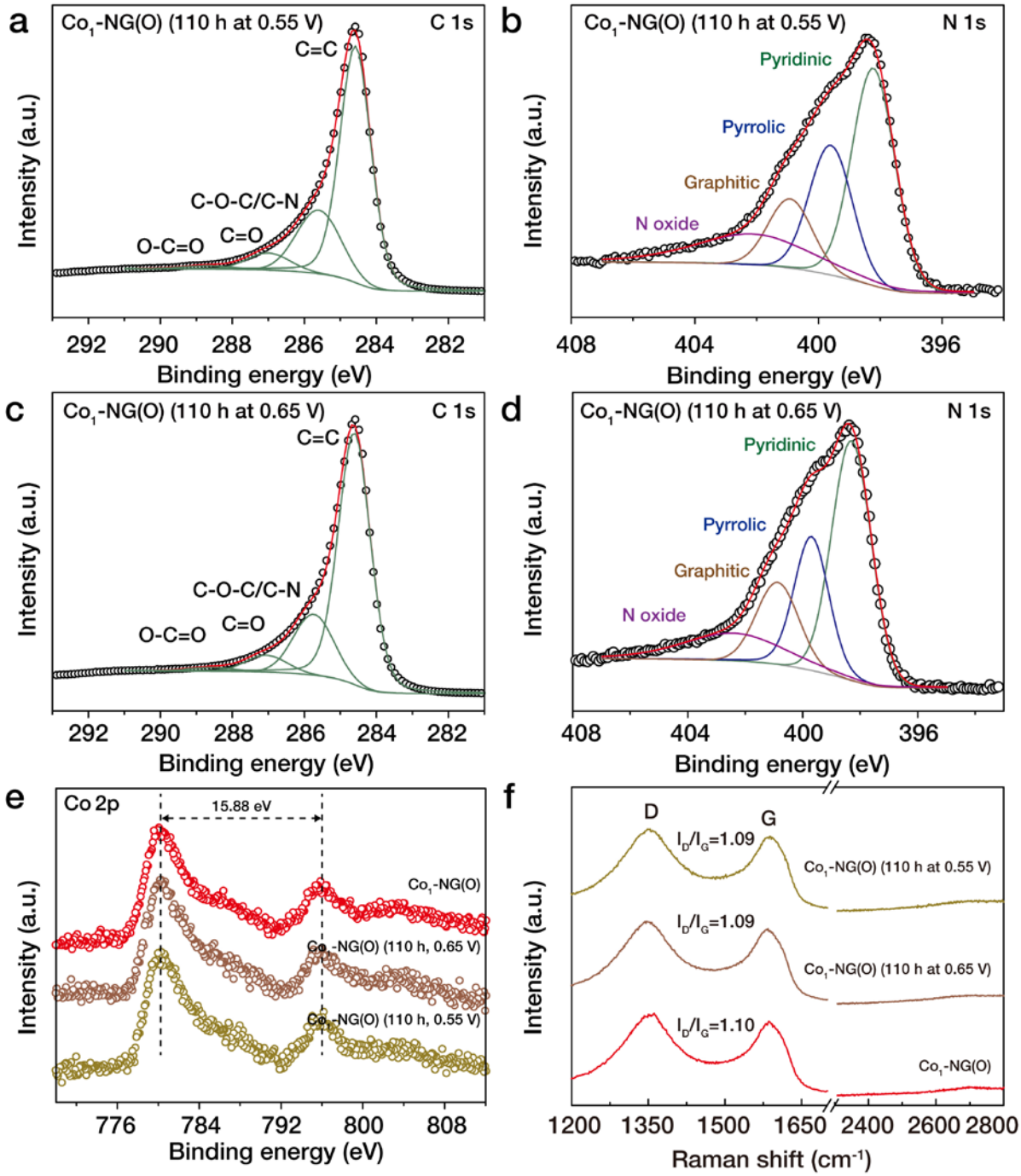

Supplementary Figure 38. (a) – (e) XPS and (f) Raman spectra analyses of Co_1-NG(O) catalyst after the stability test (chronoamperometry at 0.55 and 0.65 V vs. RHE in 0.1 M KOH for 110 h). After the stability test, it can be seen that the chemical configurations (e.g. C=C and C-N bonds) are well preserved and there is negligible structural change as confirmed by the XPS and Raman spectra analyses.

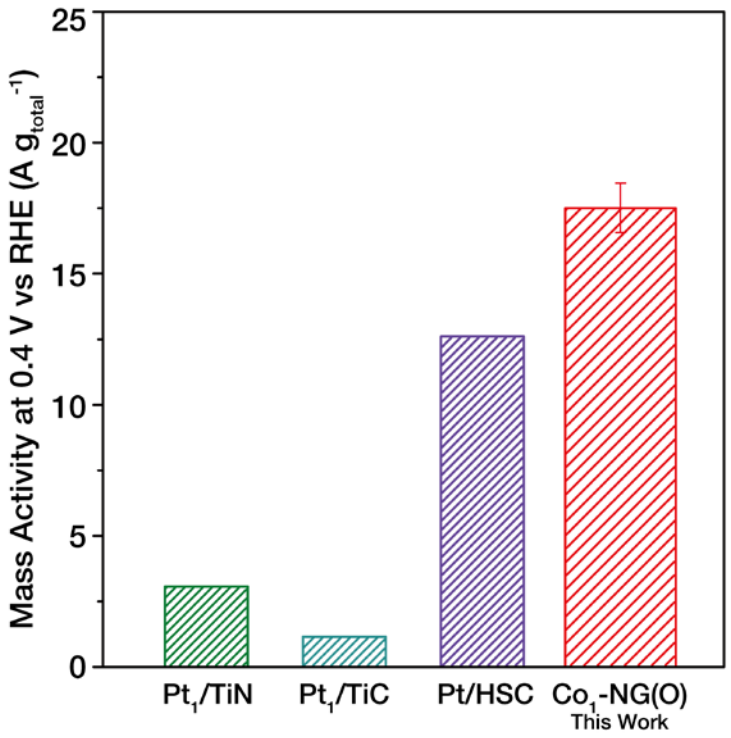

Supplementary Figure 39. Mass activity of various Pt single atom catalysts (refs. 6-8) and Co_1-NG(O) catalyst at 0.4 V (versus RHE) in 0.1 M $HClO_4$ electrolyte. The activity of Pt/HSC was measured with RRDE at 900 rpm in the previous study, so we corrected that value approximately by 1.25 times to compare and evaluate fairly, following the Levich equation (see Methods).

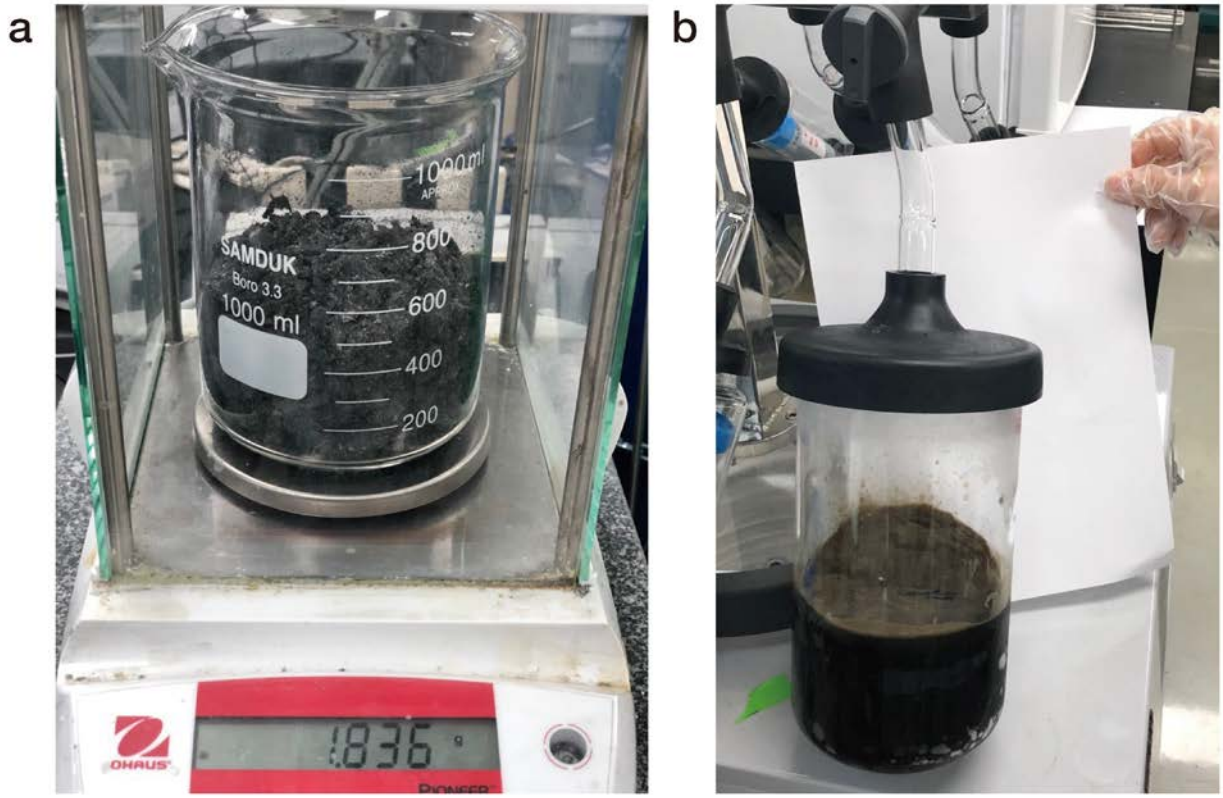

Supplementary Figure 40. Large-scale synthesis of Co_1-NG(O) SAC. (**a**) As synthesized Co_1-NG(O) (1.84 g) from a single pot and (**b**) the image of Co-adsorbed graphene oxide during dry freezing step.

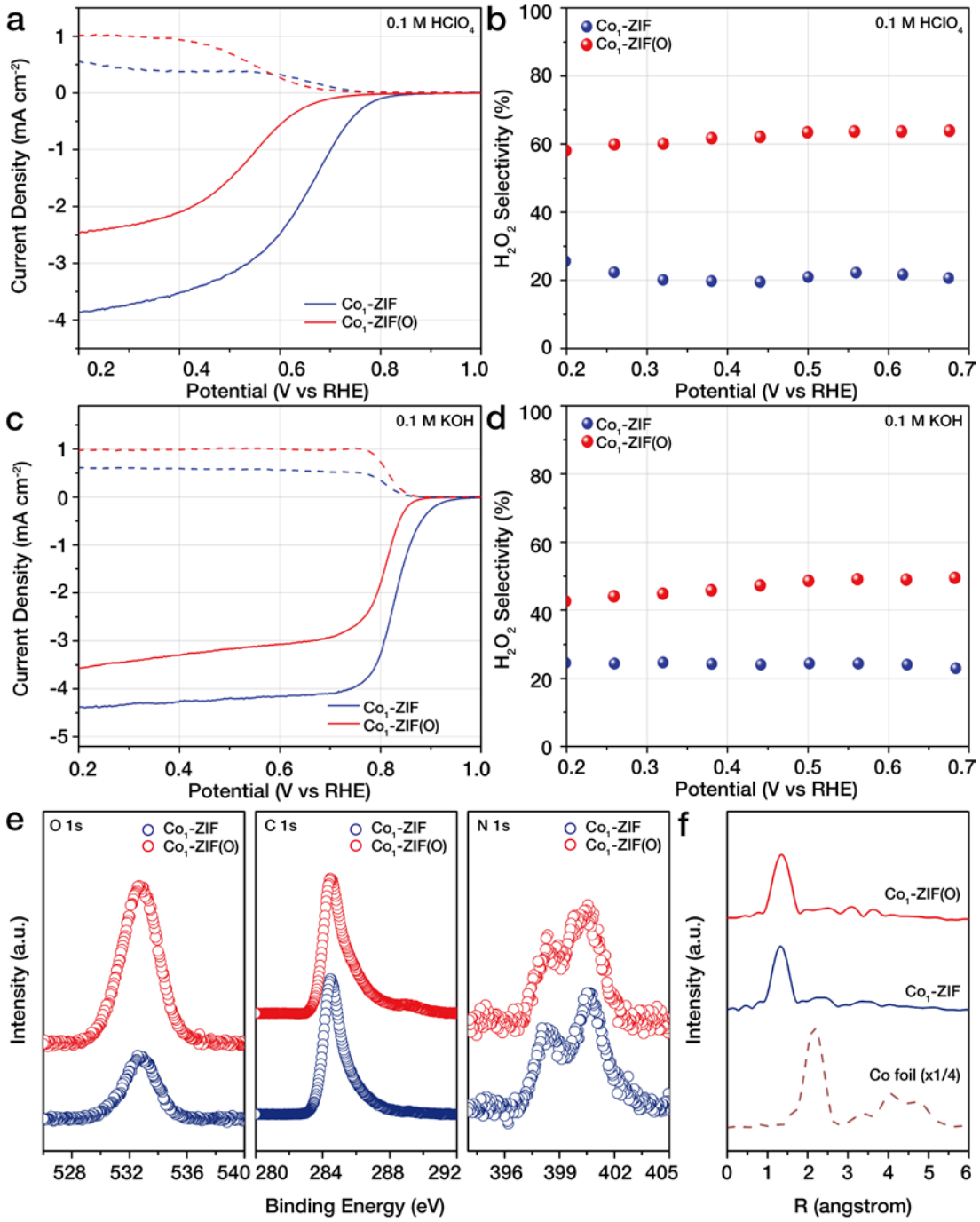

Supplementary Figure 41. (a), (b) Electrocatalytic performance of Co single atom catalysts stabilized on ZIF-derived carbons for oxygen reduction to H_2O_2 in acidic (0.1 M $HClO_4$) and (c), (d) in alkaline (0.1 M KOH) media. (e) O 1s, C 1s, and N 1s XPS spectra and (f) Co K-edge k^3-weighted FT-EXAFS of Co_1-ZIF and Co_1-ZIF(O)n real space. We applied our concepts to zeolitic imidazolate framework (ZIF)-derived carbon. ZIF-derived carbon decorated with Co single atoms (Co_1-ZIF) was first synthesized (see Methods). Based on the concept of modified Hummers method (ref. 10), we carried out acid and mild H_2O_2 treatment to synthesize oxidized Co_1-ZIF catalyst (Co_1-ZIF(O)). The oxygen content increased from 4.6 at% to 10.3 at%. Co_1-ZIF(O) showed improvement in ring current and the H_2O_2 selectivity, demonstrating that our concept is applicable to other high surface area carbon such as ZIF-derived carbon.

Table S1. Concentration of metals measured by ICP-AES (nd: not detected).

Catalyst	Mn (wt%)	Co (wt%)	Ni (wt%)	Fe (wt%)
Graphene Oxide	2.53	nd	nd	nd
Graphene Oxide (HCl)	nd	nd	nd	nd
Co_1-NG(O)	nd	1.40	nd	nd
Co_1-NG(O) (110 h at 0.65 V)	nd	1.39	nd	nd
Co_1-NG(O) (110 h at 0.55 V)	nd	1.24	nd	nd
Ni_1-NG(O)	nd	nd	1.29	nd
Fe_1-NG(O)	nd	nd	nd	1.40

Table S2. Structural parameters extracted from the Co, Fe, and Ni K-edge EXAFS fitting of M_1-NG(O) SACs. (S_0^2=0.86)

Sample	Scattering pair	CN	R(Å)	σ^2 (10^{-3} Å^2)	ΔE_0(eV)	R factor
Co_1-NG(O)	Co-N/C	4.08	1.91	11.3	-3.95	0.00359
Co_1-NG(R)	Co-N/C	3.79	1.89	7.65	-1.14	0.00487
Fe_1-NG(O)	Fe-N/C	3.98	1.93	15.5	-1.20	0.00412
Ni_1-NG(O)	Ni-N/C	3.72	1.89	4.88	0.922	0.00442

S_0^2 is the amplitude reduction factor; CN is the coordination number; R is interatomic distance (the bond length between central atoms and surrounding coordination atoms); σ^2 is Debye-Waller factor (a measure of thermal and static disorder in absorber-scatterer distances); ΔE_0 is edge-energy shift (the difference between the zero kinetic energy value of the sample and that of the theoretical model). R factor is a measure of the quality of the EXAFS fitting.

Table S3. Summary of the TOF values of various catalysts for electrochemical H_2O_2 production.

Catalyst	Active sites	Electrolyte	TOF (s^{-1})	Ref.
Co_1-NG(O)	**Co**	**0.1 M KOH**	**3.38 (± 0.15)**	**This work**
F-mrGO	sp^2-hybridized carbon near-ring ether defects	0.1 M KOH	0.0881	2
O-CNT	-COOH and C-O-C functional groups	0.1 M KOH	0.0178	3
single atom Pt/TiN	Pt	0.1 M $HClO_4$	0.0789	6
single atom Pt/HSC	Pt	0.1 M $HClO_4$	0.117	8
Pt-Hg	Pt	0.1 M $HClO_4$	0.0263	11
Pd-Hg	Pd	0.1 M $HClO_4$	0.0733	12
Au-Pt-Ni	Au and Pt	0.1 M KOH	0.0768	13

Calculation of turnover frequency (TOF) for electrochemical H_2O_2 production

To compare the activity of various catalysts (e.g. noble / non-noble metal and non-metal catalysts), we normalized the mass activity by 1) the total weight of the catalyst and 2) the weight of the active metal component only (see Fig. 4b,c). Activity of different catalysts was also evaluated by comparing their turn over frequency (TOF) values which consider the differences in the site density of various catalysts. TOF is the total number of molecules transformed into the desired product by one active site per time. In this study, the TOF values of catalysts were calculated for the $2e^-$ ORR pathway to evaluate the efficiency of electrochemical H_2O_2 production. The equation for deriving TOF is as follows.

TOF (s^{-1}) = (number of oxygen molecules turnover) / (number of active sites) = (j/2F) / n *(6)*

j is the current density for H_2O_2 production measured from ring electrode with the collection efficiency of our RRDE setup at a given overpotential, F is the faraday constant (96,485 C mol^{-1}), and n is the number of active sites. (j/2F) stands for the total oxygen turnover in $2e^-$ ORR.

The number of oxygen molecules turnover was calculated as follows.

$$\text{(number of oxygen molecules turnover)} = j\left[\frac{\text{mA}}{cm^2}\right] \times \frac{1\,[C/s]}{1000\,[mA]} \times \frac{1\,[mol\,e^-]}{96485\,[C]} \times \frac{1\,[\,mol\,O_2]}{2\,[mol\,e^-]} \times \left(6.02 \times 10^{23}\left[\frac{atom\,O_2}{mol\,O_2}\right]\right) \quad (7)$$

The number of active sites was calculated as follows.

$$\text{(number of active sites)},\ n = L\left[\frac{mg}{cm^2}\right] \times R\,[\text{wt\%}] \times \frac{1\,[mmol]}{W\,[mg]} \times \left(6.02 \times 10^{20}\left[\frac{atom}{mmol}\right]\right) \quad (8)$$

L is the amount of catalyst loaded on the electrode, R is the weight fraction, and W is the atomic weight of the corresponding element of active sites.

In case of our Co_1-NG(O) catalyst, the relatively electron-poor cobalt atom center (1.40 wt%) can be considered as the active site, assuming all the cobalt centers participate in the ORR reaction. Then, the TOF value at 0.65 V (vs. RHE) is calculated as follows.

- (number of oxygen molecules turnover) = $1.55\ [\frac{\mathrm{mA}}{cm^2}] \times \frac{1\ [C/s]}{1000\ [mA]} \times \frac{1\ [mol\ e^-]}{96485\ [C]}$

$$\times \frac{1\ [\ mol\ O_2]}{2\ [mol\ e^-]} \times (6.02 \times 10^{23}\ [\frac{atom\ O_2}{mol\ O_2}])$$

$$= 4.84 \times 10^{15}\ [\frac{\mathrm{atom}\ O_2}{s \cdot cm^2}]$$

- (number of active sites) = $0.0100\ [\frac{mg}{cm^2}] \times 0.0140 \times \frac{1\ [mmol]}{58.933\ [mg]} \times (6.02 \times 10^{20}\ [\frac{atom\ Co}{mmol}]) =$

$1.43 \times 10^{15}\ [\frac{\mathrm{atom}\ Co}{cm^2}]$

Therefore, the TOF (s^{-1}) value for the electrochemical H_2O_2 production of Co_1-NG(O) is 3.38 (s^{-1})

Similarly, the TOF values for other catalysts (e.g. Fig. 4) have been derived and the result can be seen in Table S3. For the catalysts containing noble metals, all the noble metal centers were assumed as the active sites. Also, it has been demonstrated that the carbon atoms adjacent to several oxygen functional groups can be an active site for $2e^-$ ORR for non-metal carbon catalysts. Thus, we calculated the number of active sites on those carbon catalysts from the oxygen content of the surface.

The calculated TOF value of our Co_1-NG(O) is 3.38 (s^{-1}) which is about 2 orders of magnitude higher than those of other catalysts reported to date. Although this TOF value is likely to be overestimated as the carbon support materials might also participate in the reaction, our results clearly demonstrate that the electron-poor cobalt single atom center is responsible for the high activity towards electrochemical H_2O_2 production.

Table S4. Calculated H_2O_2 productivity of different catalysts in electrochemical or direct synthesis.

H_2O_2 production method	**Catalyst**	**H_2O_2 productivity (mmol g_{cat}^{-1} h^{-1})**	**Reference**
Electrochemical Production	**Co_1-NG(O)**	**418 (± 19)**	**This work**
	O-CNTs	111.7	3
Direct Synthesis	3wt% Pd-2wt % Sn/TiO_2	61 (0.5 wt% H_2O_2)	14
	2.5% Au-2.5% Pd/carbon	175 (1.1 wt% H_2O_2)	15
	Pd-$HHDMA_5$/C	50.4	16
	Pd_5Sn/TiO_2	120.1	17
	AuPd/1LBL	90	18

References and Notes:

1. Ramaswamy, N. & Mukerjee, S. Influence of inner- and outer-sphere electron transfer mechanisms during electrocatalysis of oxygen reduction in alkaline media. *J. Phys. Chem. C* **115**, 18015-18026 (2011).
2. Kim, H. W. et al. Efficient hydrogen peroxide generation using reduced graphene oxide-based oxygen reduction electrocatalysts. *Nat. Catal.* **1**, 282-290 (2018).
3. Lu, Z. et al. High-efficiency oxygen reduction to hydrogen peroxide catalysed by oxidized carbon materials. *Nat. Catal.* **1**, 156-162 (2018).
4. Wang, X. X., Prabhakaran, V., He, Y., Shao, Y. & Wu, G. Iron-free cathode catalysts for proton-exchange-membrane fuel cells: Cobalt catalysts and the peroxide mitigation approach. *Adv. Mater.* 1805126 (2019).
5. Li, J. et al. Atomically dispersed manganese catalysts for oxygen reduction in proton-exchange membrane fuel cells. *Nat. Catal.* **1**, 935-945 (2018).
6. Yang, S., Kim, J., Tak, Y. J., Soon, A. & Lee, H. Single-atom catalyst of platinum supported on titanium nitride for selective electrochemical reactions. *Angew. Chem. Int. End.* **55**, 2058-2062 (2016).
7. Yang, S., Tak, Y. J., Kim, J., Soon, A. & Lee, H. Support effects in single-atom platinum catalysts for electrochemical oxygen reduction. *ACS Catal.* **7**, 1301-1307 (2017).
8. Choi, C. H. et al. Tuning selectivity of electrochemical reactions by atomically dispersed platinum catalyst. *Nat. Commun.* **7**, 10922 (2016).
9. Murayama, T. & Yamanaka, I. Electrosynthesis of neutral H_2O_2 solution from O_2 and water at a mixed carbon cathode using an exposed solid-polymer-electrolyte electrolysis cell. *J. Phys. Chem. C* **115**, 5792-5799 (2011).
10. Shahriary, L. & Athawale, A. A. Graphene oxide synthesized by using modified Hummers approach. *Int. J. Renew. Energy Environ. Eng.* **2**, 58-63 (2014).
11. Siahrostami, S. et al. Enabling direct H_2O_2 production through rational electrocatalyst design. *Nat. Mater.* **12**, 1137-1143 (2013).
12. Verdaguer-Casadevall, A. et al. Trends in the electrochemical synthesis of H_2O_2: enhancing activity and selectivity by electrocatalytic site engineering. *Nano Lett.* **14**, 1603-1608 (2014).
13. Zheng, Z., Ng, Y. H., Wang, D.-W. & Amal, R. Epitaxial growth of Au–Pt–Ni nanorods for direct high selectivity H_2O_2 production. *Adv. Mater.* **28**, 9949-9955 (2016).
14. Freakley, S. J. et al. Palladium-tin catalysts for the direct synthesis of H_2O_2 with high selectivity. *Science* **351**, 965-968 (2016).
15. Edwards, J. K. et al. Switching off hydrogen peroxide hydrogenation in the direct synthesis process. *Science* **323**, 1037-1041 (2009).
16. Lari, G. M., Puértolas, B., Shahrokhi, M., López, N. & Pérez-Ramírez, J. Hybrid palladium nanoparticles for direct hydrogen peroxide synthesis: the key role of the ligand. *Angew. Chem.* **129**, 1801-1805 (2017).
17. Li, F., Shao, Q., Hu, M., Chen, Y. & Huang, X. Hollow Pd−Sn nanocrystals for efficient direct H_2O_2 synthesis: the critical role of Sn on structure evolution and catalytic performance. *ACS Catal.* **8**, 3418-3423 (2018).
18. Kanungo, S., Paunovic, V., Schouten, J. C. & D'Angelo, M. F. N. Facile synthesis of catalytic AuPd nanoparticles within capillary microreactors using polyelectrolyte multilayers for the direct synthesis of H_2O_2. *Nano Lett.* 17, 6481-6484 (2017).